UNIVERSITEIT VAN PRETORIA
UNIVERSITY OF PRETORIA
YUNIBESITHI YA PRETORIA

Vibrational modes of the wurtzite structures: ZnO, GaN and 6H-SiC

by

Ndanduleni Nephale

Submitted in partial fulfilment of the requirements for the degree

Magister Scientiae

in the faculty of Natural and Agricultural Sciences
University of Pretoria
Pretoria

Supervisor: Prof H. W Kunert

2009, 18 June

UNIVERSITEIT VAN PRETORIA
UNIVERSITY OF PRETORIA
YUNIBESITHI YA PRETORIA

DECLARATIONS

I declare that the dissertation , which I hereby submit for the degree Magister Scientiae at the University of Pretoria, is my own work and has not previously been submitted by me for a degree at this or any other institution.

Candidate's signature: . . . . Date: . . . .

ACKNOWLEDGEMENTS

I would like to thank the following persons for their help in this work:

- My supervisor, Prof H. W. Kunert and Mr A. G. Machatine who guided me through my study
- Prof D.J. Brink and Dr L. Prinsloo who helped with Photoluminescence and Raman measurements respectively.
- Mrs P. Mohlala who helped with the Infrared measurements.
- My Mother (TN Nkhumeleni) who was always being supported since I was born and my family for being encouraging through my study, you are the best.
- The financial assistance of University of Pretoria and SANHARP are really gratefully acknowledged.

Summary

Due to the technological interest of the wide band gap, high electron mobilities, thermal and chemical stability semiconductors such as GaN, ZnO and 6H SiC which can be used in semiconductor industries, high temperature, and corrosive atmosphere or irradiation. However thermodynamic, magnetic properties and lattice dynamics of these semiconductors are not well understood and are closely related to the vibrational modes.

We strongly make use of group theoretical techniques to classify the vibrational modes in crystals throughout the Brillouin zone (BZ). By determining the Lattice Modes Representations (LMR) of GaN, the number of allowed modes and their symmetries were obtained and then also applied to ZnO and 6H - SiC.
Assignments of the phonons of high symmetry points and lines through the entire BZ were done using compatibility relations. Phonons assignment due to the Time Reversal Symmetry (TRS) at $\Gamma \longrightarrow \Delta \longrightarrow A$ region was also discussed and shows the correlation with experimental results done by means of Neutron and X-Ray scattering techniques.

Raman active modes which are allowed for the crystals belong to C_{6v}^4 space group at the center of BZ were also calculated. Frequently, irradiation to most of the material leaves damaged defects and impurities on the material. Silver(Ag) implantation was done on the untreated material of 6H - SiC polytype. The process called annealing, yields to the recovering of the crystal structure or on the surface of materials.

Raman, Infrared and Photoluminescence spectroscopy were used to characterize the vibrational modes of different material (untreated, Ag implanted and annealed) at room temperature. This is possible due to the advancement of the laser technology which is widely available in laboratories.

Contents

1 Introduction 1

2 Theoretical Background 2

2.1 Lattice Modes Representations for wurtzite structure 2

2.2 Phonons assignment in ZnO, GaN and 6H-SiC semiconductors with C_{6v}^4 space group 8

2.3 Space and Time reversal symmetry 17

2.3.1 Space symmetry 17

2.3.2 Time reversal symmetry 17

2.4 Determination of the Raman active modes in crystals with the C_{6v}^4 space group $(\vec{k} \cong 0)$ 27

3 Experimental procedures 30

3.1 Raman spectroscopy 30

3.2 Infrared spectroscopy 33

3.3 Photoluminescence 35

4 Results and Discussions 37

4.1 Raman spectroscopy 37

4.2 Infrared spectroscopy 45

4.3 Photoluminescence 47

5 Conclusions 51

List of Figures

1 Arrangement of the Ga and N atoms 2
2 GaN bulk group theoretical phonon assignments of Γ modes 8
3 Phonon dispersion curves for GaN crystal of wurtzite structure, From Nipko's et al [14] 9
4 Phonons dispersion curve of symmetry point K_3 for GaN crystal 9
5 GaN bulk group theoretical phonon assignments of the Nipko's et al.[14] measured and calculated modes 16
6 Assignments of phonons in ZnO influenced by the time reversal symmetry.[16] 21
7 Phonons dispersion curves in ZnO predicted by shell model based on elastic constants and Raman spectrum, with measured frequencies. Hewat [18] 24
8 Calculated and measured phonon dispersion curves for ZnO. Thoma et al. [19] 25
9 Phonon dispersion curve of wurtzite type GaN along several high symmetry directions. Ruf et al.[20] 26
10 Energy level diagram showing the states involved in Raman signal 31
11 Schematic of basic setup of Raman spectrometer 32
12 Schematic representation of Fourier Transform Infrared (FTIR) Spectrometer 33
13 The schematic block diagram of PL spectroscopy 35
14 Raman measurements of 6H SiC, region 1 39
15 Raman measurements of 6H SiC, region 2 40
16 Raman measurements of 6H SiC, region 3 44
17 Infrared spectroscopy measurements of 6H SiC 46
18 Photoluminescence measurements of 6H SiC, region 1 49
19 Photoluminescence measurements of 6H SiC, region 2 50

List of Tables

1 The character table of high symmetry point Γ from the CDML tables . . 5
2 The character table of high symmetry point K from the CDML tables [8] 6
3 The character table of high symmetry line $\sum$ from the CDML tables [8] . 6
4 Normal modes spanned by Displacement Representations at critical high symmetry points and lines in C_{6v}^4 wurtzite 7
5 The character table of high symmetry line Λ from the CDML tables [8] . 10
6 The character table of high symmetry line K from the CDML tables [8] . 10
7 Compatibility of the C_{6v}^4 space group representations 14
8 The character table of high symmetry point A from the CDML tables . . 20
9 The character table of high symmetry point Δ from the CDML tables . . 20
10 Table used to determine the Symmetrized Vector representations 28
11 Phonons frequencies (in cm^{-1}) of the strong and weak zone center modes from Raman measurements [26] 38
12 Two phonons process in Wurtzite C_{6v}^4 41
13 Phonons frequencies of 6H - SiC $(in \pm 5\, cm^{-1})$ zone center modes from Raman measurements by Kunert et. al[27] 43

1 Introduction

We investigated the properties of vibrational modes of the semiconductors such as ZnO, GaN and 6H-SiC belonging to the wurtzite structure in order to characterize the materials. These compounds have recently received considerable attention due to their potential in the semiconductor industry.

These semiconductors have many applications in a electronics industry, a high-power, fast switching devices, ultra violet (UV), Infrared (IR) and detectors. Recently, attracted much attention in a new field in new device applications of spinotronics [1],[2],[3]. Spinotronics seeks to exploit the spin of charge carriers in conductors and its widely expected to be controlled above room temperature [4]. Most of these semiconductors can also be used in a high temperature and corrosive atmosphere or radiation environment due to their chemical stability.

However, their opto- electronic, thermodynamic, magnetic properties and lattice dynamics are still not well understood. These properties are closely related to the vibrational modes of the materials. By doping ZnO, GaN and 6H-SiC heterostructure has suggested the possibility of spin injection from ferromagnetic electrode. The desire to combine ferromagnetic and conventional semiconductor materials into new devices for the electronics industry has driven increasing interest into the study of magnetic layers suitable for spin injection in semiconductors [5]. Ion implantation is one the methods of doping in semiconductor technology and it makes the fabrication easier.[6]

There are various techniques that can probe phonons in a crystals, among them X- Ray scattering, Raman Spectroscopy (RS), Infrared Photoluminescence (PL) and neutron time-of-flight technique. In this work, we particularly use Raman, Infrared and Photoluminescence spectroscopy to characterize the vibrational modes at room temperature due to the advancement of the laser technology which is widely available in the laboratory. We strongly make use of group theoretical techniques to classify the vibrational modes in crystals throughout the Brillouin zone (BZ) [5].

2 Theoretical Background

In this chapter, we use the group theoretical approach to determine explicitly:

i) The number of allowed modes and their symmetries irreducible representations spanned by Displacement Representation (DR) at a critical point and high symmetry lines.

ii) The connectivity relations (compatibilities) throughout the entire BZ.

iii) Raman active modes at the center of BZ.

We use the CDML 1979 Tables [8] where the generators of all small wave vector space group irreducible representations (irrps) are given together with their characters. These tables are the most comprehensive ones, because they provide also all possible Kronecker Products for all space groups.

2.1 Lattice Modes Representations for wurtzite structure

The Lattice Modes Representation(LMR) also called the Displacement Representations (DR) for GaN has been derived by Kunert [7]. In this, we recall part of determinations and apply it to ZnO. Figure 1 displays the arrangement of the Ga and N atoms.

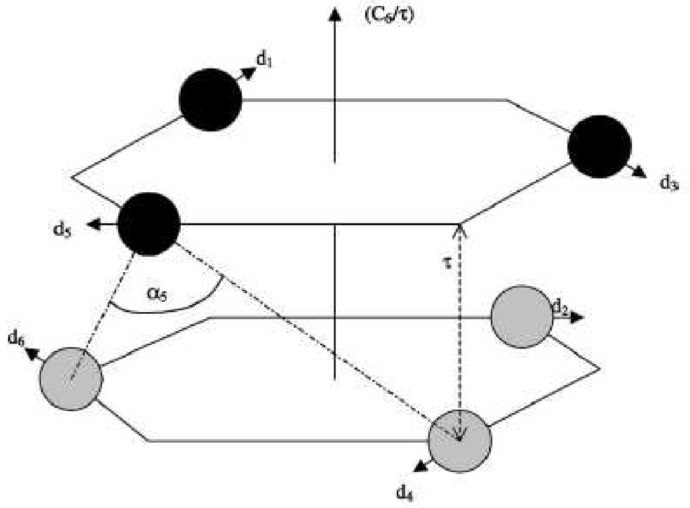

Figure 1: Arrangement of the Ga and N atoms

There are six displacements ($d_j : 1, \ldots, 6$) and six angles between corresponding atoms denoted as $\alpha_5(d_4 d_5 d_6)$, where α_5 is the angle between the atoms enumerated 4 and 6. The angles $\alpha_1(d_6 d_1 d_2)$, $\alpha_2(d_1 d_2 d_3)$, $\alpha_3(d_2 d_3 d_4)$, $\alpha_4(d_3 d_4 d_5)$, and $\alpha_6(d_5 d_6 d_1)$ are not shown for the sake of clarity.

We introduce twelve vector basis, six vector displacements and six angles between corresponding atoms (see figure 1).
Imposing symmetry operations of the C_{6v}^4 group of GaN at $\vec{k} = 0$ onto base, we obtain a set of twelve matrices of 12×12 dimensions, called DR.

For example, applying the $(C_6|00\frac{1}{2}))$ symmetry operator on the base we obtain:

$$(C_6|00\tfrac{1}{2}) \begin{bmatrix} d_1 \\ d_2 \\ d_3 \\ d_4 \\ d_5 \\ d_6 \\ \alpha_1 \\ \alpha_2 \\ \alpha_3 \\ \alpha_4 \\ \alpha_5 \\ \alpha_6 \end{bmatrix} = (d_2, d_3, d_4, d_5, d_6, d_1, \alpha_2, \alpha_3, \alpha_4, \alpha_5, \alpha_6, \alpha_1)$$

The above equation can also be written as:

$$(C_6|00\tfrac{1}{2})\begin{bmatrix} d_1 \\ d_2 \\ d_3 \\ d_4 \\ d_5 \\ d_6 \\ \alpha_1 \\ \alpha_2 \\ \alpha_3 \\ \alpha_4 \\ \alpha_5 \\ \alpha_6 \end{bmatrix} = \begin{bmatrix} A_{11} & .. & .. & .. & .. & A_{16} \\ .. & .. & .. & .. & .. & .. \\ .. & .. & .. & .. & .. & .. \\ .. & .. & .. & .. & .. & .. \\ .. & .. & .. & .. & .. & .. \\ A_{61} & .. & .. & .. & .. & A_{66} \end{bmatrix} \begin{bmatrix} d_1 \\ d_2 \\ d_3 \\ d_4 \\ d_5 \\ d_6 \\ \alpha_1 \\ \alpha_2 \\ \alpha_3 \\ \alpha_4 \\ \alpha_5 \\ \alpha_6 \end{bmatrix}$$

$$= (d_2, d_3, d_4, d_5, d_6, d_1, \alpha_2, \alpha_3, \alpha_4, \alpha_5, \alpha_6, \alpha_1)$$

It is the matter to find the matrix A. The formula above represent a set of algebric equation for matrix elements A_{ij}. By means of standard methods[8], it can be shown that matrix A is:

$$\mathrm{D}(C_6/\tau) = \begin{bmatrix} A_2 & 0 \\ 0 & A_2 \end{bmatrix}, \quad A_6 = \begin{bmatrix} 0 & 1 & 0 & 0 & 0 & 0 \\ 1 & 0 & 0 & 0 & 0 & 0 \\ 0 & 0 & 0 & 0 & 0 & 1 \\ 0 & 0 & 0 & 0 & 1 & 0 \\ 0 & 0 & 0 & 1 & 0 & 0 \\ 0 & 0 & 1 & 0 & 0 & 0 \end{bmatrix}, \quad \chi \ (C_6/\tau) = 0$$

where the symmetry operator C_6 is associated with a non-primitive translation $(00\frac{1}{2})$. Acting by all others operators on the basis we obtain the DR (twelve matrices of 12×12). The characters of the DR are listed in Table 1.

Table 1: The character table of high symmetry point Γ from the CDML tables

	E	C_6^+/τ	C_3^+	C_2/τ	C_3^-	C_6^-/τ	σ_{v1}	σ_{d2}/τ	σ_{v3}	σ_{d1}/τ	σ_{v2}	σ_{d3}/τ
g	1	2.1	3	4.1	5	6.1	19	20.1	21	22.1	23	24.1
DR	12	0	0	0	0	0	4	0	4	0	4	0
Γ_1	1	1	1	1	1	1	1	1	1	1	1	1
Γ_2	1	1	1	1	1	1	-1	-1	-1	-1	-1	-1
Γ_3	1	-1	1	-1	1	-1	-1	1	-1	1	-1	1
Γ_4	1	-1	1	-1	1	-1	1	-1	1	-1	1	-1
Γ_5	2	-1	-1	2	-1	-1	0	0	0	0	0	0
Γ_6	2	1	-1	-2	-1	1	0	0	0	0	0	0

Decomposing the DR by means of reduction formula onto irrps of the C_{6v}^4 space group, we obtain the correct number and symmetries of vibrational modes in ZnO, originating from the entire BZ [9].

The reduction formula is of the form:

$$n_v = \frac{1}{g}\sum_i g_i \chi^{v_i *}\left(g/\tau_g\right)\chi^D\left(g/\tau_g\right) \tag{1}$$

where $\chi^{v_i *}$ and χ^D are characters of the DR and irrps of ZnO respectively (see table 1).

From equation 1 at high symmetry point Γ , we obtain:

$$\Gamma \Rightarrow 2\Gamma_1 \oplus 2\Gamma_4 \oplus 2\Gamma_5 \oplus 2\Gamma_6 \tag{2}$$

for phonons with $k \cong 0$ (center of the BZ)

The relation 2 says that there are eight allowed phonons with momentum $\hbar k \cong 0$, with the symmetries $\Gamma_1, \Gamma_4, \Gamma_5, \Gamma_6$ respectively. Clearly, phonons of symmetries Γ_2 and Γ_3 are not existing in ZnO. By means of several experimental techniques such as neutron scattering, Infrared absorption and Raman spectroscopy, the energies of these phonons have been measured.

Similarly using equation 1 and the character tables [8] for other high symmetry point and lines we decompose DR onto irrps of ZnO for $k \neq 0$ (see Appendix 1). For instance for high point symmetry K (table 2) and line $\sum$ (table 3), we obtain:

$$K \Rightarrow 2K_1 \oplus 2K_2 \oplus 4K_3$$

and

$$\sum \Rightarrow 8\sum_1 \oplus 8\sum_2$$

Table 2: The character table of high symmetry point K from the CDML tables [8]

g	1	3	5	20.1	22.1	24.1
K_1	1	1	1	1	1	1
K_2	1	1	1	-1	-1	-1
K_3	2	-1	-1	0	0	0

Table 3: The character table of high symmetry line $\sum$ from the CDML tables [8]

g	1	23.1
$\sum_1$	1	1
$\sum_2$	1	-1

Consider the high symmetry point K in the BZ. From the table 4, follows that at this point there are eight phonons of symmetries $2K_1$, $2K_2$ and $4K_3$. For the high symmetry lines Λ and T we have $6\Lambda_1$, $6\Lambda_2$ and $6T_1$, $6T_2$ vibrational modes respectively [29].

Proceeding this way, we find the number and allowed symmetries of phonons in ZnO listed in table 4. Detailed calculations are shown in the Appendix 1.

Table 4: Normal modes spanned by Displacement Representations at critical high symmetry points and lines in C_{6v}^4 wurtzite

$$
\begin{array}{ccl}
\Gamma & : & 2\Gamma_1 \oplus 2\Gamma_4 \oplus 2\Gamma_5 \oplus 2\Gamma_6 \\
A & : & 2A_1 \oplus 2A_4 \oplus 2A_5 \oplus 2A_6 \\
\Delta & : & 2\Delta_1 \oplus 2\Delta_4 \oplus 2\Delta_5 \oplus 2\Delta_6 \\
H & : & 2H_1 \oplus 2H_2 \oplus 4H_3 \\
P & : & 2P_1 \oplus 2P_2 \oplus 4P_3 \\
K & : & 2K_1 \oplus 2K_2 \oplus 4K_3 \\
L & : & 4L_1 \oplus 4L_2 \oplus 4L_3 \oplus 4L_4 \\
M & : & 4M_1 \oplus 4M_2 \oplus 4M_3 \oplus 4M_4 \\
U & : & 4U_1 \oplus 4U_2 \oplus 4U_3 \oplus 4U_4 \\
R & : & 8R_1 \oplus 4R_2 \\
\sum & : & 8\sum_1 \oplus 4\sum_2 \\
Q & : & 6Q_1 \oplus 6Q_2 \\
S & : & 6S_1 \oplus 6S_2 \\
\Lambda & : & 6\Lambda_1 \oplus 6\Lambda_2 \\
T & : & 6T_1 \oplus 6T_2
\end{array}
$$

The decomposition of the derived Lattice Modes Representations(LMR) yields the finite number of allowed phonons and their symmetries. Our table 4 can be quite useful in verification of the experimental measurement for phonons dispersion curves but it cannot help us to do the phonons assignment. In section 2.2, we will discuss phonons assignment of semiconductors with C_{6v}^4 space group in detail.

2.2 Phonons assignment in ZnO, GaN and 6H-SiC semiconductors with C_{6v}^{4} space group

In this section, we assign phonons of high symmetry point and lines through the entire BZ, using compatibility relations. Nipko's et al [14] have measured phonons frequencies in GaN by means of time - of - flight neutron spectroscopy. The results are showed in figure 4. Clearly, using reduction formula and table 1 in section 2.1, we see that at high symmetry point Γ, we have eight phonons. The Γ's phonons are assigned, where the short lines showed correspond with the dimensions of the symmetry as follows (see figure 2).

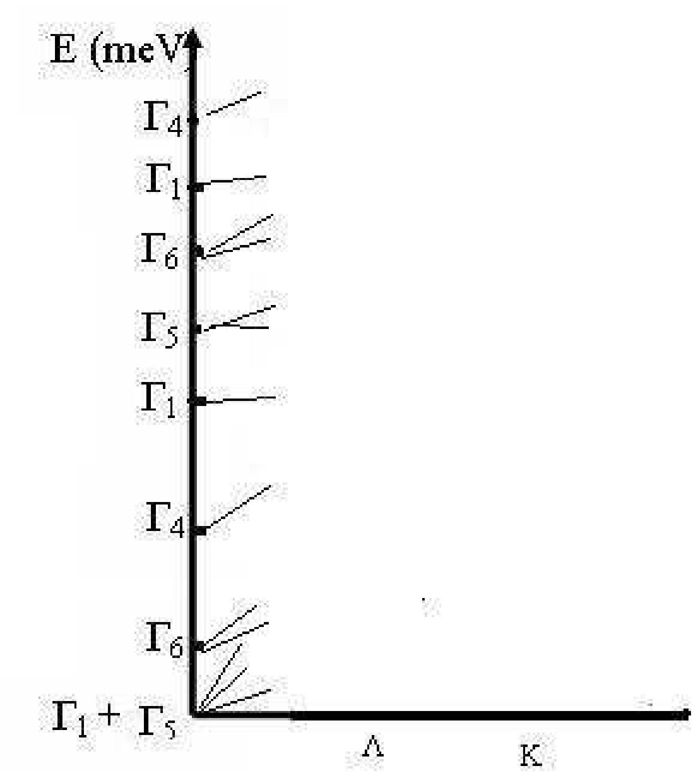

Figure 2: GaN bulk group theoretical phonon assignments of Γ modes

Figure 3 exhibits the phonons dispersion curve measured by time-of-flight neutron scattering, where the phonons are not yet assigned.

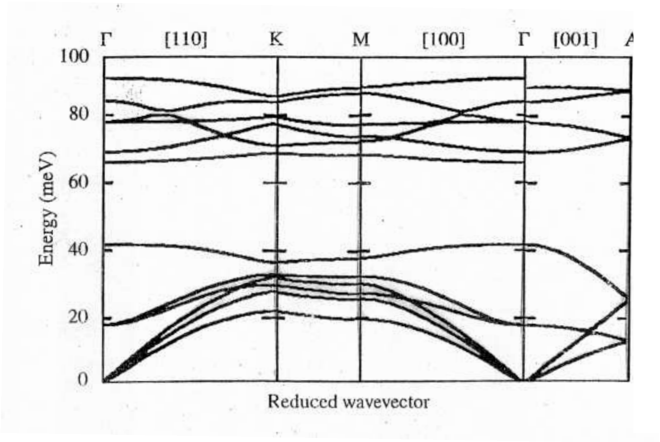

Figure 3: Phonon dispersion curves for GaN crystal of wurtzite structure, From Nipko's et al [14]

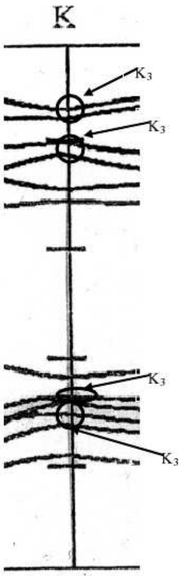

Figure 4: Phonons dispersion curve of symmetry point K_3 for GaN crystal

Next, we assign K's phonons from high symmetry points Γ passing via the low symmetry line Λ. Clearly, the splitting occurs due to lowering of symmetry.

Using the reduction formula 3 and the character tables of high symmetries points and lines [8], we can derive the compatibility relations between the irreducible representations (irrps) of the high symmetry point and lines presented in Table 7.

The reduction formula is of the form:

$$a_\mu = \frac{1}{g} \sum g_i \chi^\sigma \left(g/\tau_g\right) \chi^\mu \left(g/\tau_g\right) \tag{3}$$

where χ^σ is the character of high symmetry point, while χ^μ is the character of low symmetry lines, for example $\Gamma \longrightarrow \Lambda$, $K \longrightarrow \Lambda$, $M \longrightarrow \sum$, etc... From compatibility relations, the exact number and symmetries of phonons originating from the entire BZ with $k \neq 0$ can be obtained.

For example, compatibility from high symmetry point Γ to low symmetry line Λ can be calculated using table 1 (for χ^{Γ}), table 5 (for χ^{Λ}) and reduction formula (equation 3).

Table 5: The character table of high symmetry line Λ from the CDML tables [8]

g	1	24.1
Λ_1	1	1
Λ_2	1	-1

Table 6: The character table of high symmetry line K from the CDML tables [8]

g	1	3	5	20.1	22.1	24.1
K_1	1	1	1	1	1	1
K_2	1	1	1	-1	-1	-1
K_3	2	-1	-1	0	0	0

Equation 3 can be formulated as:

For Λ_1

$$a_{\Lambda_1} = \frac{1}{g} \sum_j \chi^{\Gamma_j} (g/\tau_g)\, \chi^{\Lambda_1} (g/\tau_g) \tag{4}$$

where (g/τ_g) is 1 and 24.1, and j= 1, . . . 6

For Γ_1:

$a_{\Lambda_1} = \frac{1}{2}\left[1(1) + 1(1)\right] = 1$

For Γ_2:

$a_{\Lambda_1} = \frac{1}{2}\left[1(1) + 1(-1)\right] = 0$

For Γ_3:

$a_{\Lambda_1} = \frac{1}{2}\left[1(1) + 1(1)\right] = 1$

For Γ_4:

$a_{\Lambda_1} = \frac{1}{2}\left[1(1) + (-1)(1)\right] = 0$

For Γ_5:

$a_{\Lambda_1} = \frac{1}{2}\left[2(1) + 0(1)\right] = 1$

For Γ_6:

$a_{\Lambda_1} = \frac{1}{2}\left[2(1) + 0(1)\right] = 1$

And for Λ_2, the reduction formula (eq. 3) can be formulated as follows:

$$a_{\Lambda_2} = \frac{1}{g}\sum_{ij} \chi^{\Gamma_j}\left(g/\tau_g\right)\chi^{\Lambda_2}\left(g/\tau_g\right) \tag{5}$$

where (g/τ_g) is 1 and 24.1, and j= 1,2 . . . 6

For Γ_1:

$a_{\Lambda_2} = \frac{1}{2}\left[1(1) + 1(-1)\right] = 0$

For Γ_2:

$a_{\Lambda_2} = \frac{1}{2}\left[1(1) + (-1)(-1)\right]$

$a_{\Lambda_2} = 1$

For Γ_3:

$a_{\Lambda_2} = \frac{1}{2}\left[1(1) + 1(-1)\right] = 0$

For Γ_4:

$a_{\Lambda_2} = \frac{1}{2}\left[1(1) + (-1)(-1)\right] = 1$

For Γ_5:

$a_{\Lambda_2} = \frac{1}{2}\left[2(1) + 0(-1)\right] = 1$

For Γ_6:

$a_{\Lambda_2} = \frac{1}{2}\left[2(1) + 0(-1)\right] = 1$

Clearly,

$\Gamma_5 \longrightarrow \Lambda_1 \oplus \Lambda_2$ and $\Gamma_6 \longrightarrow \Lambda_1 \oplus \Lambda_2$

Therefore the compatibility relations between Γ's and Λ's yields:

$\Gamma_{1,3} \longrightarrow \Lambda_1, \Gamma_{2,4} \longrightarrow \Lambda_2$, $\Gamma_5 \longrightarrow \Lambda_1 \oplus \Lambda_2$ and $\Gamma_6 \longrightarrow \Lambda_1 \oplus \Lambda_2$

Similarly, for high symmetry point K (table 6) and low symmetry line Λ, the reduction formula (eq. 3) can be formulated as follows:

$$a_{\Lambda_1} = \frac{1}{g}\sum_{j} \chi^{K_j}\left(g/\tau_g\right)\chi^{\Lambda_1}\left(g/\tau_g\right) \tag{6}$$

where (g/τ_g) is 1 and 24.1, and j= 1,2.3

For K_1:

$a_{\Lambda_1} = \frac{1}{2}\left[1(1) + 1(1)\right] = 1$

For K_2:

$a_{\Lambda_1} = \frac{1}{2}\left[1(1) + 1(-1)\right] = 0$

For K_3:

$a_{\Lambda_1} = \frac{1}{2}\left[2(1) + 0(1)\right] = 1$

And for Λ_2, the reduction formula (eq. 3) can be formulated as follows:

$$a_{\Lambda_2} = \frac{1}{g}\sum_{ij} \chi^{K_j}\left(g_i/\tau_g\right)\chi^{\Lambda_2}\left(g_i/\tau_g\right) \tag{7}$$

where (g_j/τ_g) is 1 and 24.1, and j= 1,2,3

For K_1:

$$a_{\Lambda_2} = \tfrac{1}{2}\left[1(1) + 1(-1)\right] = 0$$

For K_2:

$$a_{\Lambda_2} = \tfrac{1}{2}\left[1(1) + (-1)(-1)\right] = 1$$

For K_3:

$$a_{\Lambda_2} = \tfrac{1}{2}\left[2(1) + 0(-1)\right] = 1$$

Therefore the compatibility relations between K's and Λ's yields:

$$K_1 \longrightarrow \Lambda_1, K_2 \longrightarrow \Lambda_2, K_3 \longrightarrow \Lambda_1 \oplus \Lambda_2$$

By repeating the same for all other high symmetry points and high symmetry lines, we can derive the compatibility relations of the C_{6v}^4 space group which is shown in Table 7.

Table 7: Compatibility of the C_{6v}^4 space group representations

$\Gamma \longrightarrow \Lambda$: $\Gamma_{1,3} \longrightarrow \Lambda_1, \Gamma_{2,4} \longrightarrow \Lambda_2, \Gamma_{5,6} \longrightarrow \Lambda_1 \oplus \Lambda_2$
$\Gamma \longrightarrow \sum$: $\Gamma_{1,4} \longrightarrow \sum_1, \Gamma_{2,3} \longrightarrow \sum_2, \Gamma_{5,6} \longrightarrow \sum_1 \oplus \sum_2$
$\Gamma \longrightarrow M$: $\Gamma_1 \longrightarrow M_1, \Gamma_2 \longrightarrow M_2, \Gamma_3 \longrightarrow M_3, \Gamma_4 \longrightarrow M_1, \Gamma_5 \longrightarrow M_1 \oplus M_2,$
$\Gamma_6 \longrightarrow M_1 \oplus M_2$
$\Gamma \longrightarrow K$: $\Gamma_{1,3} \longrightarrow K_1, \Gamma_{2,4} \longrightarrow K_2, \Gamma_{5,6} \longrightarrow K_3$
$\Gamma \longrightarrow T$: $\Gamma_{1,3} \longrightarrow T_1, \Gamma_{2,4} \longrightarrow T_2, \Gamma_{5,6} \longrightarrow T_1 \oplus T_2$
$A \longrightarrow R$: $A_{1,4} \longrightarrow R_1, A_{2,3} \longrightarrow R_2, A_{5,6} \longrightarrow R_3$
$A \longrightarrow Q$: $A_{1,3} \longrightarrow Q_1, A_{2,4} \longrightarrow Q_2, A_{5,6} \longrightarrow Q_3$
$A \longrightarrow L$: $A_1 \longrightarrow L_1, A_2 \longrightarrow L_2, A_3 \longrightarrow L_3, A_4 \longrightarrow L_4, A_5 \longrightarrow L_1 \oplus L_2,$
$A_6 \longrightarrow L_3 \oplus L_4$
$A \longrightarrow H$: $A_{1,3} \longrightarrow H_1, A_{2,4} \longrightarrow H_2, A_{5,6} \longrightarrow H_3$
$L \longrightarrow R$: $L_{1,4} \longrightarrow R_1, L_{2,3} \longrightarrow R_2$
$L \longrightarrow S$: $L_{1,3} \longrightarrow S_1, L_{2,4} \longrightarrow S_2$
$H \longrightarrow Q$: $H_1 \longrightarrow Q_1, H_2 \longrightarrow Q_2, H_3 \longrightarrow Q_1 \oplus Q_2$
$H \longrightarrow S$: $H_1 \longrightarrow S_1, H_2 \longrightarrow S_2, H_3 \longrightarrow S_1 \oplus S_2$
$M \longrightarrow \sum$: $M_{1,4} \longrightarrow \sum_1, M_{2,3} \longrightarrow \sum_2$
$M \longrightarrow T$: $M_{1,3} \longrightarrow T_1, M_{2,4} \longrightarrow T_2$
$K \longrightarrow \Lambda$: $K_1 \longrightarrow \Lambda_1, K_2 \longrightarrow \Lambda_2, K_3 \longrightarrow \Lambda_1 \oplus \Lambda_2$
$K \longrightarrow T$: $K_1 \longrightarrow T_1, K_2 \longrightarrow T_2, K_3 \longrightarrow T_1 \oplus T_2$
$K \longrightarrow M$: $K_1 \longrightarrow M_1 \oplus M_3, K_2 \longrightarrow M_2 \oplus M_4,$
$K_3 \longrightarrow M_1 \oplus M_2 \oplus M_3 \oplus M_4$

Calculations of the derived compatibility relations can be checked as follows: Considering the highest in energy, Γ_4 phonon (first from the top on figure 5 at high symmetry point Γ) and lower in energy, Γ_1 (second from the top on the same figure). From the figure, phonons $\Gamma_4 \longrightarrow \Lambda_2$ and $\Gamma_1 \longrightarrow \Lambda_1$. While on the other hand, phonons from K_3 (the top phonons at high symmetry point K), $K_3 \longrightarrow \Lambda_1 \oplus \Lambda_2$ which leads back to Γ_4 and Γ_1.

From Nipko's[14] experimental data (figure 5) follows that there are 12 phonons with different energies at symmetry point K. Our rigid calculations in section 2.1, table 4

yield only eight phonons at symmetry point K which is $2K_1$,$2K_2$, and $4K_3$.
Therefore, the top symmetry lines Λ_1 and Λ_2 modes must join each other at point K yielding one phonon at K_3 symmetry: $K_3 \longrightarrow \Lambda_1 \oplus \Lambda_2$.

Similarly for the phonons at Γ_5 and Γ_6, the lines must join each other at the symmetry point K also yielding another one phonon of K_3 symmetry. The other two phonons at K_3 will be the joints of symmetry lines from Γ_6 and $\Gamma_1 \oplus \Gamma_6$
Similarly, the T_1 and T_2 modes on high symmetry line T must join each other at symmetry point K yielding K_3 mode: $K_3 \longrightarrow T_1 \oplus T_2$. The four circles at the point K indicate four two - fold degenerate K_3 vibrational modes (see figure 4). The small energy gaps between branches at K_3 are most presumably caused by experimental error or impurities on the sample.

We did not assign $\mathbf{k}_\Delta$ and $\mathbf{k}_A$ phonons on figure 5. In Section 2.3, we list the irrps of $G^{\mathbf{k}}_\Delta$ and $G^{\mathbf{k}}_A$ factor space groups. Instead of the symmetry groups $G^{\mathbf{k}}_\Delta$ and $G^{\mathbf{k}}_A$, we then handle with the antiunitary groups which will be discussed in details later.
Considering Nipko's et al. [14] measurement done for GaN by means of time-of-flight neutron scattering (see figure 5). Clearly, this group theoretical method can verify the experimentally measured vibrational modes in a crystal.
From figure 5 , it follows that the measured frequencies of all allowed phonons modes by these technique and their group theoretical phonon assignments are available. The energies of eight allowed symmetry phonons modes have been measured by time-of-flight neutron scattering technique (see figure 3).

However the measurement of Γ phonons by this technique yield inaccurate measurements for phonons with $k = 0$.
The best technique to be used for the phonons with $k = 0$ is Raman spectroscopy. We took several Raman spectrum of ZnO and 6H - SiC crystals. Our frequency slightly differs with Nipko's et al. In order to discuss the Raman spectrum, we introduce or recall short theory of Raman Scattering in Section 2.4.

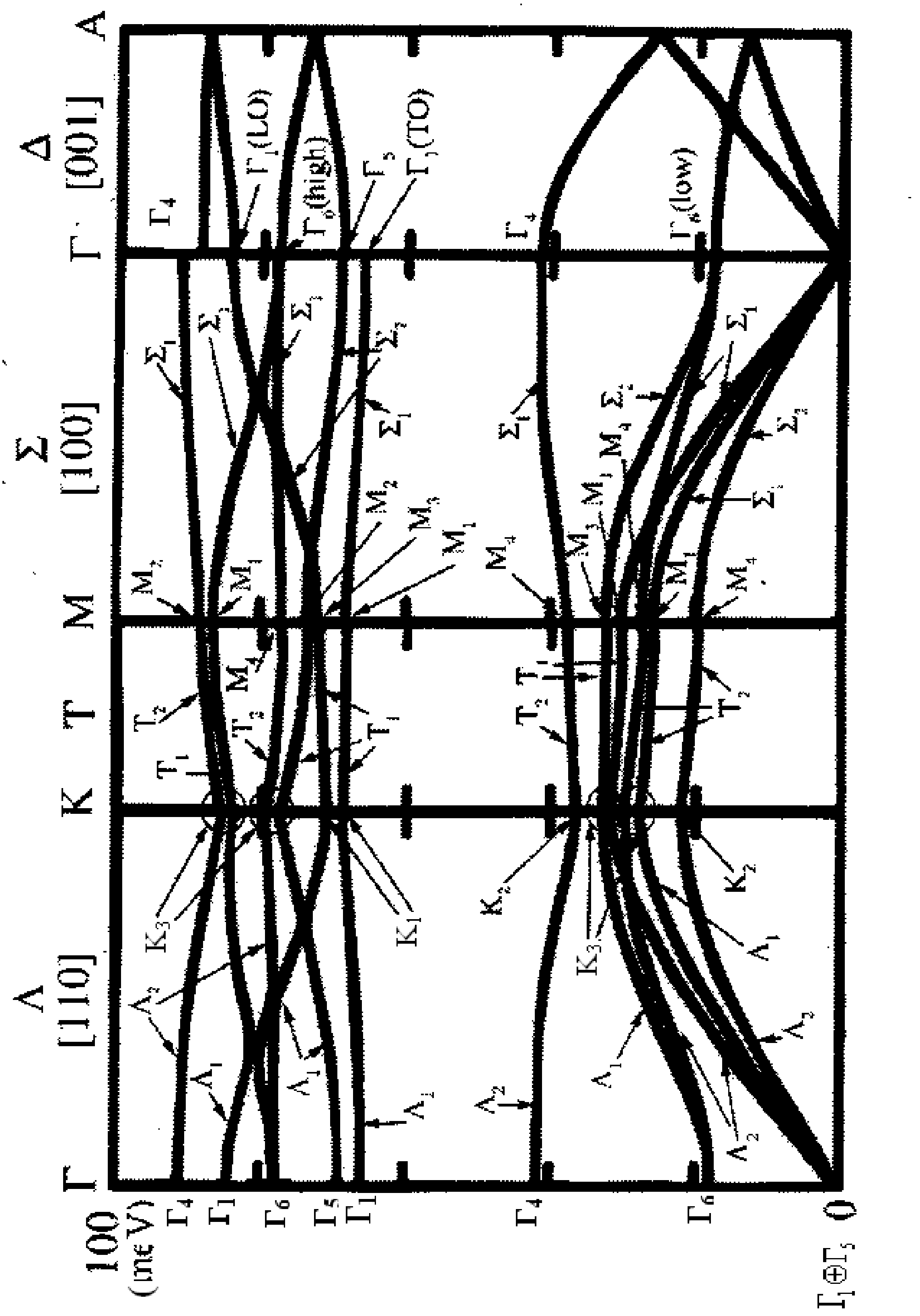

Figure 5: GaN bulk group theoretical phonon assignments of the Nipko's et al.[14] measured and calculated modes

2.3 Space and Time reversal symmetry

2.3.1 Space symmetry

The Hamiltonian for a lattice vibration on a crystal is invariant with respect to the symmetry operators $\{g_i|\tau_g\} \equiv \{g\}$ of a crystal space group $G^{\mathbf{k}}$ ($\{g_i|\tau_g\} \equiv \{g\} \in G^{\mathbf{k}}$)

$$\hat{g}\hat{H}\hat{g}^{-1} = \hat{H} \tag{8}$$

For $\hat{H}\psi_i = E\psi_i$

$$\hat{g}\left(\hat{H}\psi_i\right) = \hat{g}\left(E\psi_i\right) \tag{9}$$

$$\hat{H}\left(\hat{g}\psi_i\right) = E\left(\hat{g}\psi_i\right) \tag{10}$$

but

$$\hat{g}\psi_i = \sum_j \psi_j D_{ji}(g) \tag{11}$$

where D_{ji} are the matrix elements of an irreducible representation (irrps) $D(g) \equiv D$ of the space group $G^{\mathbf{k}}$. Clearly the ψ are the eigenfunctions of the Hamiltonian and simultaneously are the basis of the irrps D.

Consequently the vibrational modes of a crystal are classified according to irrps D. This follows from the space symmetry. However, there might be an existence of so - called Time reversal symmetry (TRS) in some crystals.

2.3.2 Time reversal symmetry

Consider a general time dependent Schroedinger equation in the absence of spin orbit coupling and external magnetic field, which is suitable for lattice vibrations excitations. In this case the Hamiltonian for phonons is real.

$$H\psi_i = i\hbar\left(\partial/\partial t\right)\psi_i = E\psi_i \tag{12}$$

Replacing $t \longrightarrow -t$ and taking complex conjugate of the above equation we get:

$$H^*\psi_i^* = i\hbar\left(\partial/\partial t\right)\psi_i^* = E\psi_i^* \tag{13}$$

Clearly, ψ_i^* are also eigenfunctions of Hamiltonian H as ψ_i (equation 10). Consequently, we are dealing with two set of wave functions: ψ_i and ψ_i^*.
On the other hand ψ_i are the basis functions of D(g) irrps and ψ_i^* are the basis functions of $D^*(g)$ irrps. The total basis (ψ_i, ψ_i^*) transforms according to joint irrps $D \oplus D^*$. Therefore, the degeneracy of the phonons modes have been doubled.
In order to determine whether in a crystal the TRS is present or not, one has to investigate all irrps of a crystal and find out which of those are complex.

Forbenius and Schur [17], derived a criteria for real and complex irrps.

$$(1/|g|)\sum_g \chi(g^2) = \begin{cases} 1 \quad case\,(a) & D\,is\,real \\ 0 \quad case\,(b) & D\,and\,D^* are\,complex\,and\,inequivalent \\ -1 \quad case\,(c) & D\,and\,D^*\,are\,complex\,and\,equivalent \end{cases} \tag{14}$$

where $|g|$ is the order of a given group G. If the sum of the characters of squares of the group elements is equal to the order of the group $|g|$, then the representations (reps) D are real; if the sum is $-|g|$, then the reps are equivalent to its conjugate; and if the sum vanishes the reps D and D^* are complex and inequivalent.[17]
In summary, the cases (b) and (c) lead to an extra degeneracy of phonons due to the TRS.

Using Forbenius and Schur criteria and the CDML [8] Tables, we have investigated all irrps of the C_{6v}^4 space group and obtain the following:

i) $\Gamma_{1,2,3,4,5,6}$, $M_{1,2,3,4}$, $K_{1,2,3}$, $\sum_{1,2}$, $T_{1,2,}$, H_3. Real reps, which means no extra degeneracy.

ii) $A_{1,2,3,4,5,6}$, $\Delta_{1,2,3,4,5,6}$, $L_{1,2,3,4}$, $U_{1,2,3,4}$, $P_{1,2,3}$, $S_{1.2}$. Complex reps which means extra degeneracy occurs.

iii) $R_{1,2}$. Complex reps, which also means extra degeneracy.

According to the calculations, the Δ and A phonons are influenced by the time reversal symmetry (TRS). We have shown that at high symmetry point A the reps spanned by modes are $2A_1$, $2A_4$, $2A_5$, $2A_6$ and at high symmetry line Δ the reps spanned by modes are $2\Delta_1$, $2\Delta_4$, $2\Delta_5$, $2\Delta_6$ symmetries.

The presence of TRS at symmetry point A and symmetry line Δ requires classification of modes according to $A \oplus A^*$ and $\Delta \oplus \Delta^*$ reps. Using compatibility relations the resulting mode's assignment is:

i) Point Γ, from the bottom to the top: $\Gamma_1 \oplus \Gamma_5$, Γ_6, Γ_4, Γ_5, Γ_6, Γ_4 and Γ_1
ii) Point A, from the bottom to the top: $A_5 \oplus (A_5)^*$, $A_1 \oplus (A_1)^*$, $A_5 \oplus (A_5)^*$, $A_1 \oplus (A_1)^*$
iii) Line Δ: the dispersion curves connect the points Γ and A when going from the bottom to the top on the A axis side: Δ_5, $(\Delta_5)^*$, Δ_1, $(\Delta_1)^*$, Δ_5, $(\Delta_5)^*$, $(\Delta_1)^*$ and Δ_1

Table 8: The character table of high symmetry point A from the CDML tables

g/τ_g	1	2.1	3	4.1	5	6.1	19	20.1	21	22.1	23	24.1
A_1	1	i	1	i	1	i	1	i	1	i	1	i
A_2	1	i	1	i	1	i	-1	$-i$	-1	$-i$	-1	$-i$
A_3	1	$-i$	1	$-i$	1	$-i$	-1	i	-1	i	-1	i
A_4	1	$-i$	1	$-i$	1	$-i$	1	$-i$	1	$-i$	1	$-i$
A_5	$\begin{pmatrix}1 & 0\\0 & 1\end{pmatrix}$	$\begin{pmatrix}i\omega^* & 0\\0 & i\omega\end{pmatrix}$	$\begin{pmatrix}\omega & 0\\0 & \omega^*\end{pmatrix}$	$\begin{pmatrix}i & 0\\0 & i\end{pmatrix}$	$\begin{pmatrix}\omega^* & 0\\0 & \omega\end{pmatrix}$	$\begin{pmatrix}i\omega & 0\\0 & i\omega^*\end{pmatrix}$	$\begin{pmatrix}0 & -i\\i & 0\end{pmatrix}$	$\begin{pmatrix}0 & -\omega^*\\\omega & 0\end{pmatrix}$	$\begin{pmatrix}0 & -i\omega\\i\omega^* & 0\end{pmatrix}$	$\begin{pmatrix}0 & -i\\i & 0\end{pmatrix}$	$\begin{pmatrix}0 & -i\omega\\i\omega & 0\end{pmatrix}$	$\begin{pmatrix}0 & -\omega\\\omega^* & 0\end{pmatrix}$
$A_6 = A_5^*$	$\omega = exp(2\pi i/3)$											

Table 9: The character table of high symmetry point Δ from the CDML tables

g/τ_g	1	2.1	3	4.1	5	6.1	19	20.1	21	22.1	23	[illegible]
Δ_1	1	$1.T$	1	$1.T$	1	$1.T$	1	$1.T$	1	$1.T$	1	[illegible]
Δ_2	1	$1.T$	1	$1.T$	1	$1.T$	-1	$-1.T$	-1	$-1.T$	-1	$-1.T$
Δ_3	1	$-1.T$	1	$-1.T$	1	$-1.T$	-1	$1.T$	-1	$1.T$	-1	$1.T$
Δ_4	1	$-1.T$	1	$-1.T$	1	$-1.T$	1	$-1.T$	1	$-1.T$	1	$-1.T$
Δ_5	$\begin{pmatrix}1 & 0\\0 & 1\end{pmatrix}$	$\begin{pmatrix}T\omega^* & 0\\0 & T\omega\end{pmatrix}$	$\begin{pmatrix}\omega & 0\\0 & \omega^*\end{pmatrix}$	$\begin{pmatrix}T & 0\\0 & T\end{pmatrix}$	$\begin{pmatrix}\omega^* & 0\\0 & \omega\end{pmatrix}$	$\begin{pmatrix}T\omega & 0\\0 & T\omega^*\end{pmatrix}$	$\begin{pmatrix}0 & T^2\\T^2 & 0\end{pmatrix}$	$\begin{pmatrix}0 & T\omega^*\\T\omega & 0\end{pmatrix}$	$\begin{pmatrix}0 & -\omega T^2\\\omega^* T^2 & 0\end{pmatrix}$	$\begin{pmatrix}0 & T\\T & 0\end{pmatrix}$	$\begin{pmatrix}0 & -\omega T^2\\\omega T^2 & 0\end{pmatrix}$	$\begin{pmatrix}0 & \omega T\\\omega^* T & 0\end{pmatrix}$
$\Delta_6 = (\Delta_5)^*$	$\omega = exp(2\pi i/3)$, $T = exp(i\pi\alpha)$											

From the reps provided in tables 8 and 9, it follows that $(A_1)^* = A_4$, $(A_5)^* = A_6$, $(\Delta_1)^* = \Delta_4$ and $(\Delta_5)^* = \Delta_6$ for high symmetry point A and for symmetry line Δ respectively [13].

These are consistent with the number of modes at Γ, A, and Δ with their symmetries obtained from Lattice modes representation (LMR).

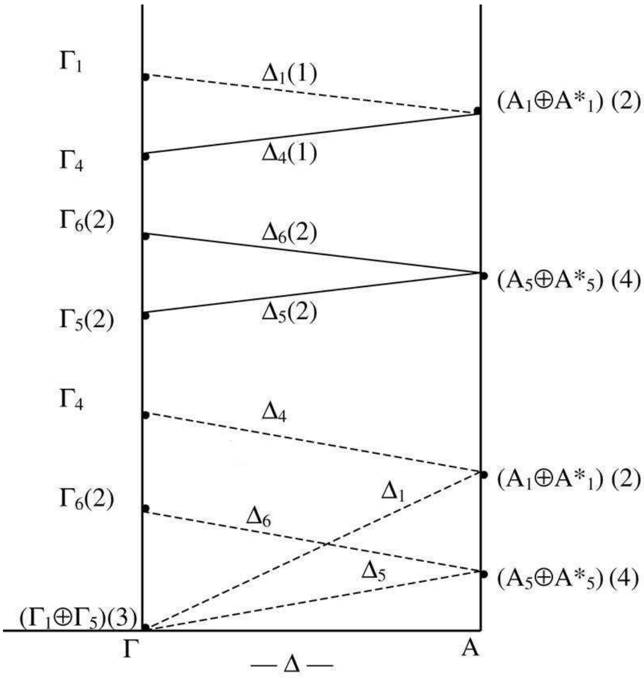

Figure 6: Assignments of phonons in ZnO influenced by the time reversal symmetry.[16]

Figure 6 displays the schematic dispersion curves $\Gamma \longrightarrow \Delta \longrightarrow A$ region of BZ subjected to TRS in wurtzite crystal. The numbers on the brackets indicate the degree of degeneracy. For example: representation A_1 and $(A_1)^*$ are both one fold degenerate, then $A_1 \oplus (A_1)^*$ becomes two fold degenerate.

For simplicity, the straight lines are used to show the phonons from one symmetry point to another. Generally, the frequencies of the modes Γ, Δ and A point may shift for different compounds under the space group C_{6v}^4/T, but the connection between Γ and A points will be kept by Δ's experimental phonon data.

The shifting may cause more accidental degeneracy. The existence of experimentally measured modes which generate dispersion curves Δ_5, Δ_6, Δ_1, Δ_4 and four phonons modes on A axis $2(A_5 \oplus A_6)$, $2(A_1 \oplus A_4)$ evidently proves the presence of the TRS in wurtzite crystals.

Due to the TRS, phonons at high symmetry point A with reps A_1 and A_4 will be represented with joint $A_1 \oplus (A_1)^*$ with two fold degenerate while the phonons at reps A_5 and A_6 will be represented with joint $A_5 \oplus (A_5)^*$ with four fold degenerate. These lead us to two degenerate pairs $2(A_1 \oplus A_1^*)$, $2(A_5 \oplus A_5^*)$ which proves the presence of TRS (see figure 6).

In figure 6, two of the phonons at high symmetry line Δ joins each other at high symmetry point A. For example, phonons Δ_1 and Δ_4 at high symmetry line Δ which are not degenerate joins each other at $A_1 \oplus A_1^*$. Phonon $A_1 \oplus A_1^*$ is a two fold time reversal degenerate. In other words, the phonons generated by reps with low degeneracy combines to give high degeneracy. While the phonons by reps with high degeneracy split into reps with low degeneracy, for example, at high symmetry point A, $2(A_5 \oplus A_5^*)$, four fold degenerate split into two phonons with reps of two fold degenerate each at high symmetry line Δ which are Δ_5 and Δ_6.

Lets consider an experimental results done by different techniques (neutron time-of-flight,inelastic neutron scattering and X-Ray scattering) with GaN and ZnO crystals.

Consider the experimental measurement done by Nipko's [14] with time-of-flight neutron scattering technique at $\Gamma \longrightarrow \Delta \longrightarrow A$ region (figure 5). There are four phonons $A \oplus A^*$ modes of high symmetry point A and eight phonons Δ modes at symmetry line Δ. Their measured energies can be read from figure 3. We can relate our calculations under TRS and the experimental phonon dispersions curve measured by this technique. Two phonons at high symmetry point Γ also joins each other at high symmetry point A passing via high symmetry line Δ.

Similarly, the experimental measurement (figure 7 and 8) by Hewat[18] and Thoma[19] using inelastic neutron scattering technique evidently proves the presence of TRS in ZnO at $\Gamma \longrightarrow \Delta \longrightarrow A$ region. On figure 8 on Δ symmetry line there are experimental points. The joint of two phonons from high symmetry point Γ at symmetry point A can be related to TRS in both figures. The phonons dispersions curve also agrees with the calculations as well as phonon dispersion curve shown in figure 6.

Ruf[20] used the different technique from Hewat and Thoma, which is X - Ray scattering technique in wurtzite type GaN. The phonon dispersion along the several high symmetry was also measured. Considering the $\Gamma \longrightarrow \Delta \longrightarrow A$ region in figure 9, we can evidently prove the joining of two phonons at the high symmetry point A due to the TRS. Again, the experimental results agree with the calculations and phonons dispersion curve in figure 6.

Different techniques used to measure phonons frequencies of wurtzite- type semiconductors yields the same results at $\Gamma \longrightarrow \Delta \longrightarrow A$ region. Therefore, the joining of the phonons at high symmetry point A are evidently influenced with TRS and phonon assignments presented in figure 6 is valid for phonons with wurtzite structures.

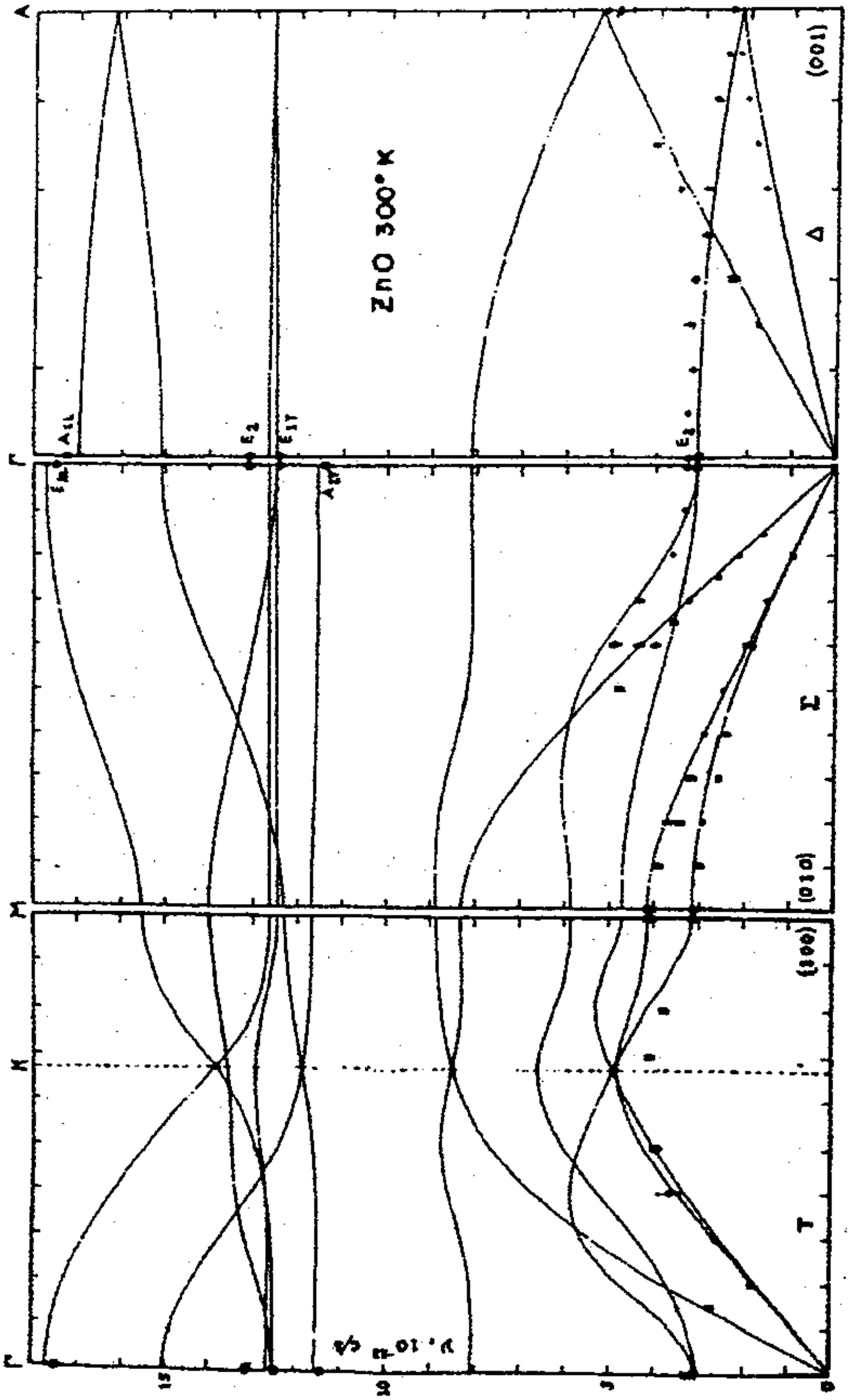

Figure 7: Phonons dispersion curves in ZnO predicted by shell model based on elastic constants and Raman spectrum, with measured frequencies. Hewat [18]

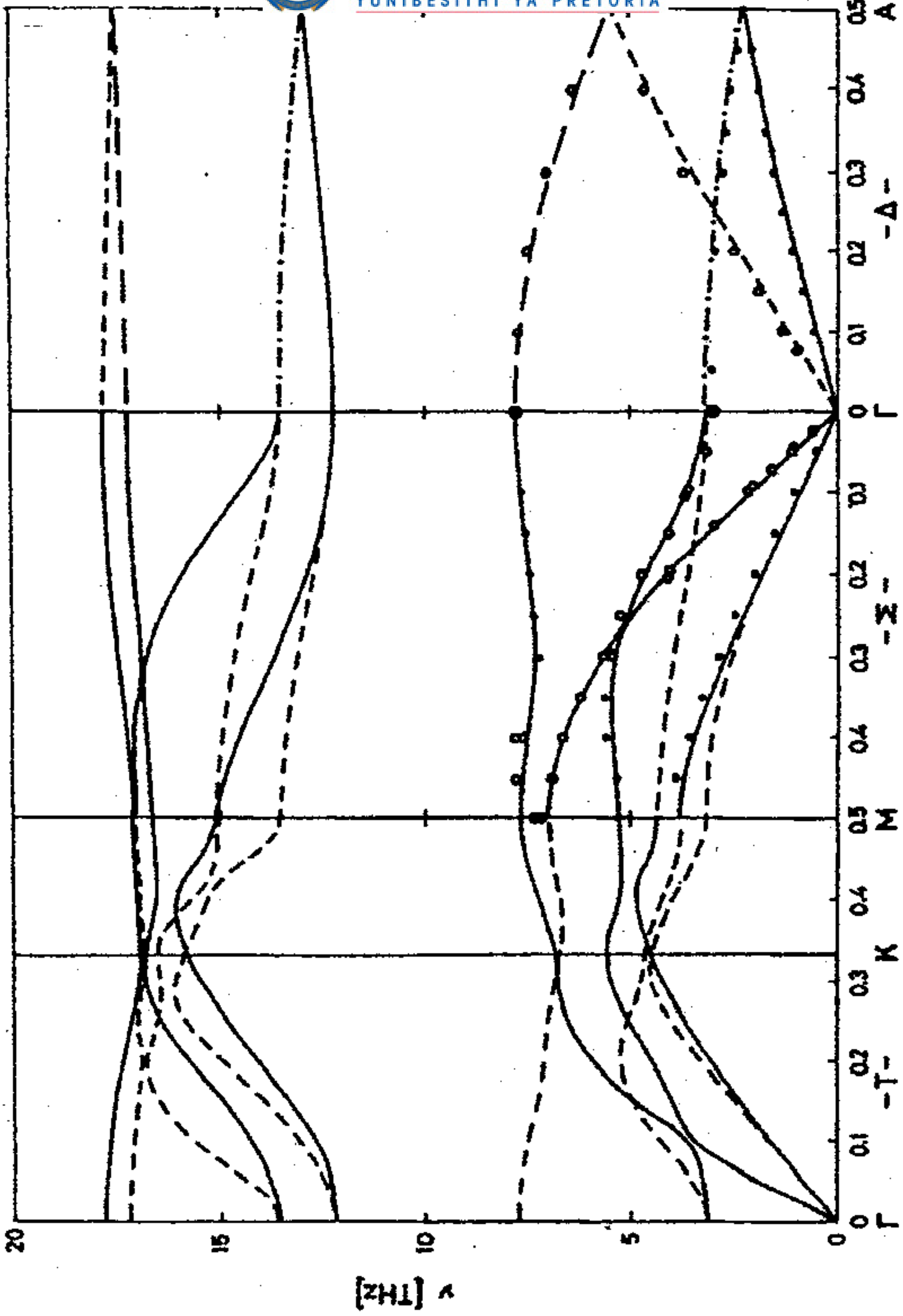

Figure 8: Calculated and measured phonon dispersion curves for ZnO. Thoma et al. [19]

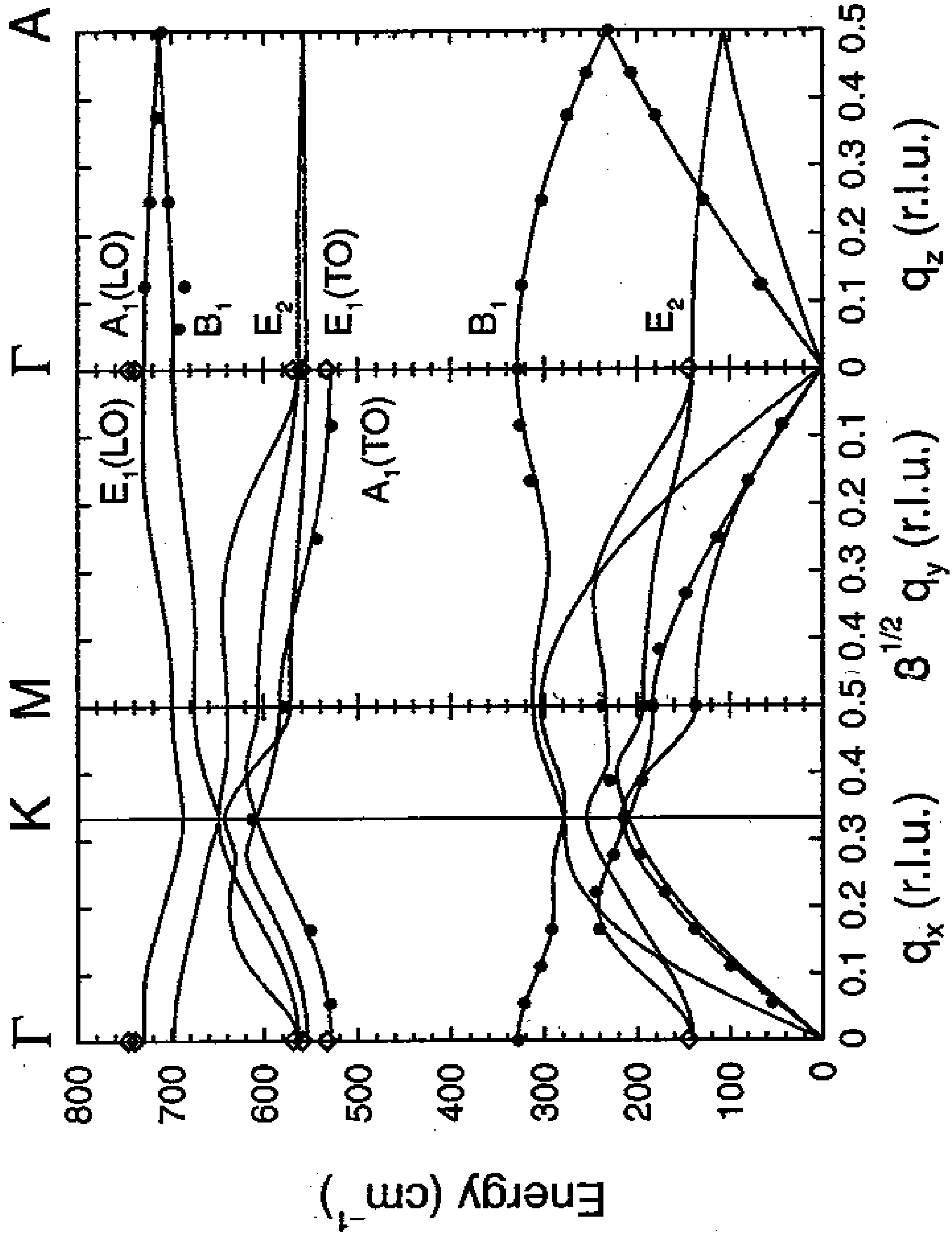

Figure 9: Phonon dispersion curve of wurtzite type GaN along several high symmetry directions. Ruf et al.[20]

2.4 Determination of the Raman active modes in crystals with the C_{6v}^4 space group ($\vec{k} \cong 0$)

Figures 5,7,8 and 9 shows experimental measurement by Nipko, Hewat, Thoma and Ruf by means of Neutron time of flight, inelastic neutron and X - Ray scattering techniques. These techniques provide accurate frequencies of measurement with longer momenta $\hbar\mathbf{k}$. How ever, these techniques are not able measure the frequencies of long wavelength phonons ($k \cong 0$, Γ center of BZ). The best techniques to measure this frequencies is Raman and Infrared scattering.

Raman scattering and infrared scattering spectra of a crystal can be used to determine the frequencies of phonon modes of a crystal. The number, symmetry type, and selection rules for the phonon modes of a crystal are determined by its space group. Where the orientation of the crystal axes relative to the polarization of the incident and scattered or absorbed photon is known, these selection rules can be used to identify the symmetry of an observed vibrational modes.

We use the CDML 1979 Tables [8] where the generators of all small wave vector space group irrps are given together with their characters.
The vector representations (VR) is based the cartesian coordinates (x,y,z). For the C_{6V}^4 space group the VR is $\Gamma_1 \oplus \Gamma_6$. See Appendix 2 for the calculations of symmetrized Vector representations.

The Raman active modes (RAMs) follows from the decomposition of the symmetrized square of the vector representation $[V \oplus V]_{(2)}$ (SVR) into irreducible representation of the C_{6v} point group. Since the Raman scattering tensor is symmetric, we split the Kronecker Products (KP) of vector representation $V \otimes V$ onto symmetrized and antisymmetrized parts. Only irreducible representations contained in the symmetrized KP are Raman active modes.

The symmetrized square of vector representation is of the form:

$$[\chi(g/\tau_g) \times \chi(g/\tau_g)]_{sym} = \frac{1}{2}\left[(\chi(g/\tau_g))^2 + \chi(g/\tau_g)^2\right] \tag{15}$$

To determine the characters of Vector representations (VR), we take the trace of the standard matrices of Hexagonal group from CDML [8]. Table 10 shows the calculations of the characters of square symmetrized vector representations .

Table 10: Table used to determine the Symmetrized Vector representations

g	1	2	3	4	5	6	19	20	21	22	23	24
g^2	1	3	5	1	3	5	1	1	1	1	1	1
$\chi(g)$	3	2	0	-1	0	2	1	1	1	1	1	1
$(\chi(g))^2$	9	4	0	1	0	4	1	1	1	1	1	1
$\chi(g^2)$	3	0	0	3	0	0	3	3	3	3	3	3
$\left[(\chi(g))^2 + \chi(g^2)\right]$	12	4	0	4	0	4	4	4	4	4	4	4
$\frac{1}{2}\left[(\chi(g))^2 + \chi(g^2)\right]$	6	2	0	2	0	2	2	2	2	2	2	2

To determine which irrps are contained in symmetrized square of vector representations, we use the reduction formula and our calculated character table (Table 10.

The reduction formula is of the form:

$$a_\mu = \frac{1}{g}\sum_i [\chi(g/\tau_g) \times \chi(g/\tau_g)]_{sym}\, \chi^{\Gamma_i}(g/\tau_g) \tag{16}$$

where $[\chi(g/\tau_g) \times \chi(g/\tau_g)]_{sym}$ is the character of the symmetrized VR and χ^{Γ_i} the character of the high symmetry point Γ, with $i = 1, 2 \ldots, 6$.

Using table 1 (for the character of Γ, χ^{Γ}), table 10 (for the character of symmetrized VR, $[\chi(g/\tau_g) \times \chi(g/\tau_g)]_{sym}$) and reduction formula (equation 16), we obtain:

$$[(\Gamma_1 \oplus \Gamma_6) \otimes (\Gamma_1 \oplus \Gamma_6)]_{(2)} = 2\Gamma_1 \oplus \Gamma_5 \oplus \Gamma_6$$

The instance calculations are presented in Appendix 3.

Therefore, for C_{6v}^4 space group crystals, we deal with six Raman active modes at the zone center of the Brillouin Zone ($\vec{k} = 0$) , which are: Γ_1 (TO), Γ_1 (LO), Γ_5 (TO), Γ_5 (LO), Γ_6 (high) and Γ_6 (low), since Γ_5 and Γ_6 are two fold degenerate.

Where TO and LO stands for Transverse Optic and Longitudinal optic respectively Results of the experimental measurements done by Raman spectroscopy and will be presented in Chapter 4.

3 Experimental procedures

3.1 Raman spectroscopy

Raman scattering measurements on a crystals obtains information about their lattice vibration frequencies. Raman scattering is a weak effect and requires a powerful sharp line source of radiation [21]. In this experiment, the Ar laser source was used.

To determine the lattice vibration frequencies of the crystal, light absorption and light scattering experiments are often carried out.

The electric field E_0cosω_0t of the incident light causes a dipole moment μ:

$$\mu = \alpha E_0 cos\omega_0 t \tag{17}$$

within the molecule, where α denotes the polarizability tensor of the molecule. The modulated moment μ will have a frequencies $\omega_0 \pm \omega_s$ and the light emitted will have those shifted frequencies. This process is not allowed for all the vibration modes and only those modes which can generate components of the polarizability tensor by molecular deformation can be Raman active[22].

The number of the Raman active and IR active modes for the material can be predicted by group theory once the lattice structure and its symmetry are specified. The number of the optically active modes is calculated by the decomposition of the irrps into symmetrized VR as already discussed.

Raman scattering is an inelastic scattering phenomenon of photons by phonons or electrons in materials. Photons with energies different from that of incident light are scattered when materials are irradiated with monochromatic light. The scattered light is very weak and we need special spectrometers that is designed to eliminate strong Rayleigh light [23].

If there is a significant excitation of vibrational excited states of the scattering molecules, then it also possible to observe scattering at frequencies above the incident frequency as the vibrational energy is added to the incident photon energy called anti stokes lines which are general weaker.

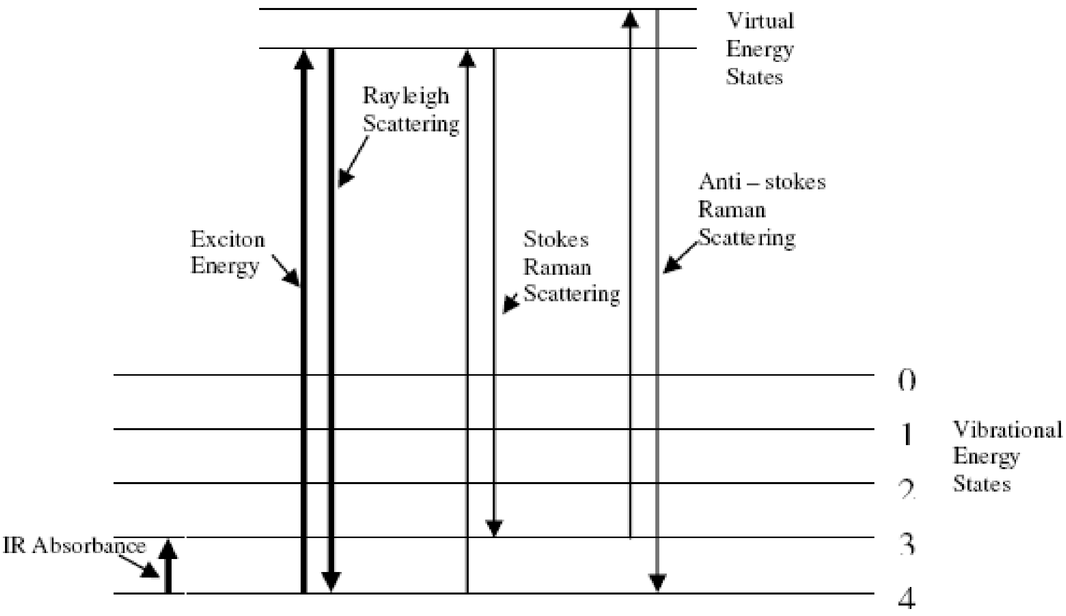

Figure 10: Energy level diagram showing the states involved in Raman signal

Raman scattering can also involve rotational transitions of the molecule from which scattering occurs.

Since the Raman effect depends upon the porazibility of the molecule, it can be observed for molecules which have no net dipole moment and therefore produces no pure rotational spectrum.

Raman spectroscopy yields high accuracy of the energies of phonons at $k \cong 0$ and offers several advantages for microscopic analysis. Raman spectra can be collected for a very small volume (less than 1 μm in diameter); these spectra allow the identification of different polytypes.

Raman spectroscopy is associated with scattering of radiation than absorption of radiation process by the sample. See schematic basic setup on the figure below.

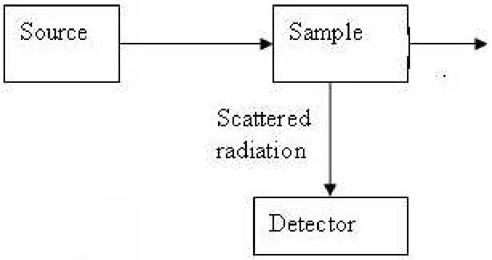

Figure 11: Schematic of basic setup of Raman spectrometer

Typically, a sample is illuminated with a laser beam. Light from the illuminated spot is collected by a lens and sent through a monochromator. Wavelengths close to the laser line, due to elastic Rayleigh scattering, are filtered out while the rest of the collected scattered light from the sample is dispersed onto a detector.

The Raman spectra may change by changing the frequency of the excitation laser. When the excitation energy is close to an energy of the high optical absorption, the Raman Intensity is enhanced, and this affect is known as the resonant Raman effect.
The Raman effect is the appearance of the weak lines in the spectrum of light scattered by the substance which has been illuminated by monochromatic light with angular frequency ω. The weak Raman sidebands are detected with a double monochromatic scanning spectrometer and a sensitive photomultiplier tube (PMT) which is cooled to reduce its intrinsic thermal noise.

3.2 Infrared spectroscopy

Infrared spectroscopy is certainly one of the most important analytical techniques available to today's scientists. The advantage of infrared spectroscopy is that any sample in any virtually state may be studied. Infrared spectra can mainly be used to: identify minerals, analyse components and the surface of minerals, establish the orientation of components and detect phase changes.

Infrared spectroscopy is a technique based on the vibrations of the atoms of a molecule. An infrared spectrum is commonly obtained by passing infrared radiation through a sample and determining what fraction of the incident radiation is absorbed at a particular energy.

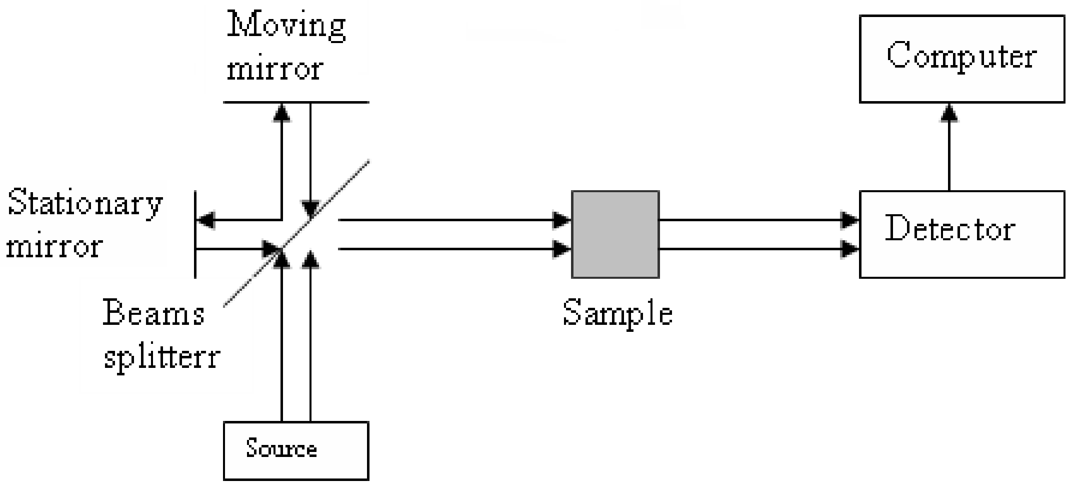

Figure 12: Schematic representation of Fourier Transform Infrared (FTIR) Spectrometer

The source produce a light and is split by the beamsplitter into two different directions, one at a right angle to the stationary mirror and the other one at a right angle to the moving mirror. The sample will absorb some of the light with the detector collecting the radiation that passes through the sample. An electrical signal is produce by the detector out and send directly to the computer to analyse.

In the case of IR absorption, only those modes which give rise to an electric dipole moment μ by molecular deformation can interact with light. Such modes are said to be IR-active and other modes, IR-inactive.
Infrared and Raman spectrum yields a partial description of the internal vibrational motion of the molecule in terms of the normal vibrations of the constituent atoms.

3.3 Photoluminescence

Photoluminescence (PL) is a technique which is used to investigate the extrinsic optical properties of the material. PL is the study of the luminescence emitted from the sample by optical excitations source of energy which is greater than the band gap of the materials.

PL spectroscopy is a non destructive technique which uses laser light as an excitation source. Materials will be bombarded with a laser light and absorbed it and excitation will occur. The excitation causes the material to go to higher energy or electronic state. Then, the material will release the energy and return to non excitation state.

In this work, we have used an Argon laser as an excitation source and excited the different types of the 6H - SiC samples. The samples were mounted and placed on the sample chamber which have to be cooled to a very low temperature. The block diagram of the PL spectroscopy is presented in the figure below:

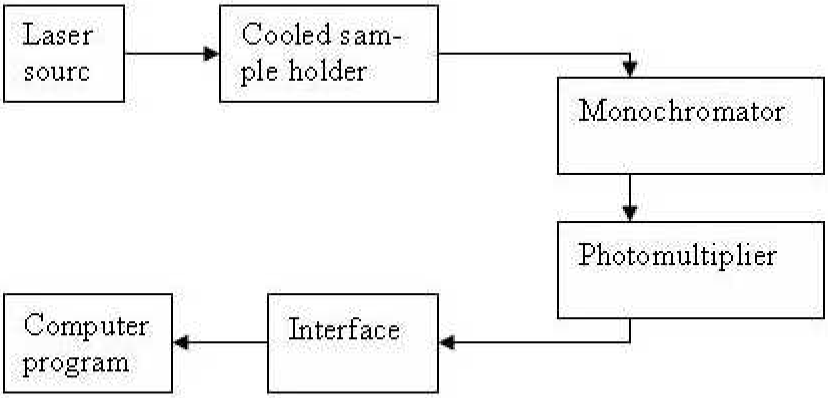

Figure 13: The schematic block diagram of PL spectroscopy

The Argon laser light has to be focused with lenses and filters to the cooled chamber which is used as the sample holder and the luminescence signal is detected by the photomultiplier tube (PMT) which produces the direct current. The direct current will be analysed by computer program which provides us with spectrum of PL.

There are several advantages of PL spectroscopy such as: to determine the band gap, the impurities and the defect on the materials, Recombination mechanisms and material quality.

4 Results and Discussions

4.1 Raman spectroscopy

Raman scattering is an inelastic scattering phenomena of photons by phonons or electron in materials. Our material 6H - SiC was irradiated with monochromatic light (Argon ion laser), and the photons with energies different from the incident light were scattered. The spectrometer which is designed to eliminate strong Rayleigh light was used as the scattered light is very weak. The dispersion signal were detected by a photomultiplier or a multichannel detector.

Different samples of 6H - SiC were used during these measurement. We are going to present the spectrum of the untreated, silver implanted and annealed material.
The spectrum was collected through different regions called region 1($100\,cm^{-1}$–$650\,cm^{-1}$), region 2 ($600\,cm^{-1} - 1100\,cm^{-1}$) and region 3 ($1000\,cm^{-1} - 1900\,cm^{-1}$).

In one phonon Raman scattering, we consider only phonons with $\mathbf{k}$=0, which are phonons near the Γ point of the BZ that are excited. As presented in chapter 2, section 2.4, Raman active modes which are excited are:

$$[(\Gamma_1 \oplus \Gamma_6) \otimes (\Gamma_1 \oplus \Gamma_6)]_{(2)} = 2\Gamma_1 \oplus \Gamma_5 \oplus \Gamma_6$$

Therefore there are six Raman active modes at the zone center of the Brillouin Zone ($\vec{k} = 0$) which are: Γ_1 (TO), Γ_1 (LO), Γ_5 (TO), Γ_5 (LO), Γ_6 (high) and Γ_6 (low).

These are the first order Raman active modes which are contained in the Symmetrized Kronecker product of the V representations. A first order Raman effect is when the single phonon is created or destroyed in the scattering process.[24] In 6H - SiC there are four Raman active strong modes at $\mathbf{q} = 0$ and $x = 0$: $2\Gamma_1$ and $2\Gamma_5$. For $\mathbf{q} = 0$ and $x = 0.33$, there are twelve folded weak modes presented by Hoffmann et al. [26] and Kunert et al. [27].

Table 11: Phonons frequencies (in cm^{-1}) of the strong and weak zone center modes from Raman measurements [26]

strong mode	Ref [26]	Experimental measurements ($\pm 5\,cm^{-1}$)
$\Gamma_1(LO)$	964	968
$\Gamma_5(LO)$	970	968
$\Gamma_5(TO)$	797	797.2
$\Gamma_1(TO)$	788	787.9
weak modes		
axial o. Γ_1	889	888
planar o. Γ_6	788	787.9
Γ_5	777	?
Γ_5	769	766.7
Γ_6	769	766.7
axial a. Γ_1	508	514
Γ_1	504	504.8
planar a. Γ_6	261	265.7
Γ_5	241	241
Γ_5	236	235
Γ_6	149	149,7
Γ_6	145	143.7

Figure 14 exhibit folded Raman active modes. The mode at $514\,cm^{-1}$ can be axial a, Γ_1 while mode at $265\,cm^{-1}$ resembles planar a, Γ_6. The peaks at $315\,cm^{-1}$ and $581\,cm^{-1}$ might follow from the instrument features or might have arises from the quality of the material or the impurities on the material since they have not yet presented in the previous literature.

A small inserted figure on figure 14 shows the zoomed folded Raman mode peaks Γ_5 at $235\,cm^{-1}$ and $241\,cm^{-1}$ which cant be visualize well in the main spectrum of untreated sample and were also presented by Hoffmann et al. [26] and Kunert et al. [27] .

Figure 15 exhibit the strong Raman active modes, the mode at $968\,cm^{-1}$ can be either modes Γ_1(LO) or Γ_5(LO). Similarly, the mode at $968\,cm^{-1}$ could be either one of the following folded modes Γ_5 or Γ_6. All first order strong and weak Raman active modes were found except folded modes Γ_5 at $777\,cm^{-1}$ presented in Hoffmann et al. [26] and Kunert et al. [27] which might be caused by all those three factors presented before (instrument features, quality of the material and impurities on the material).

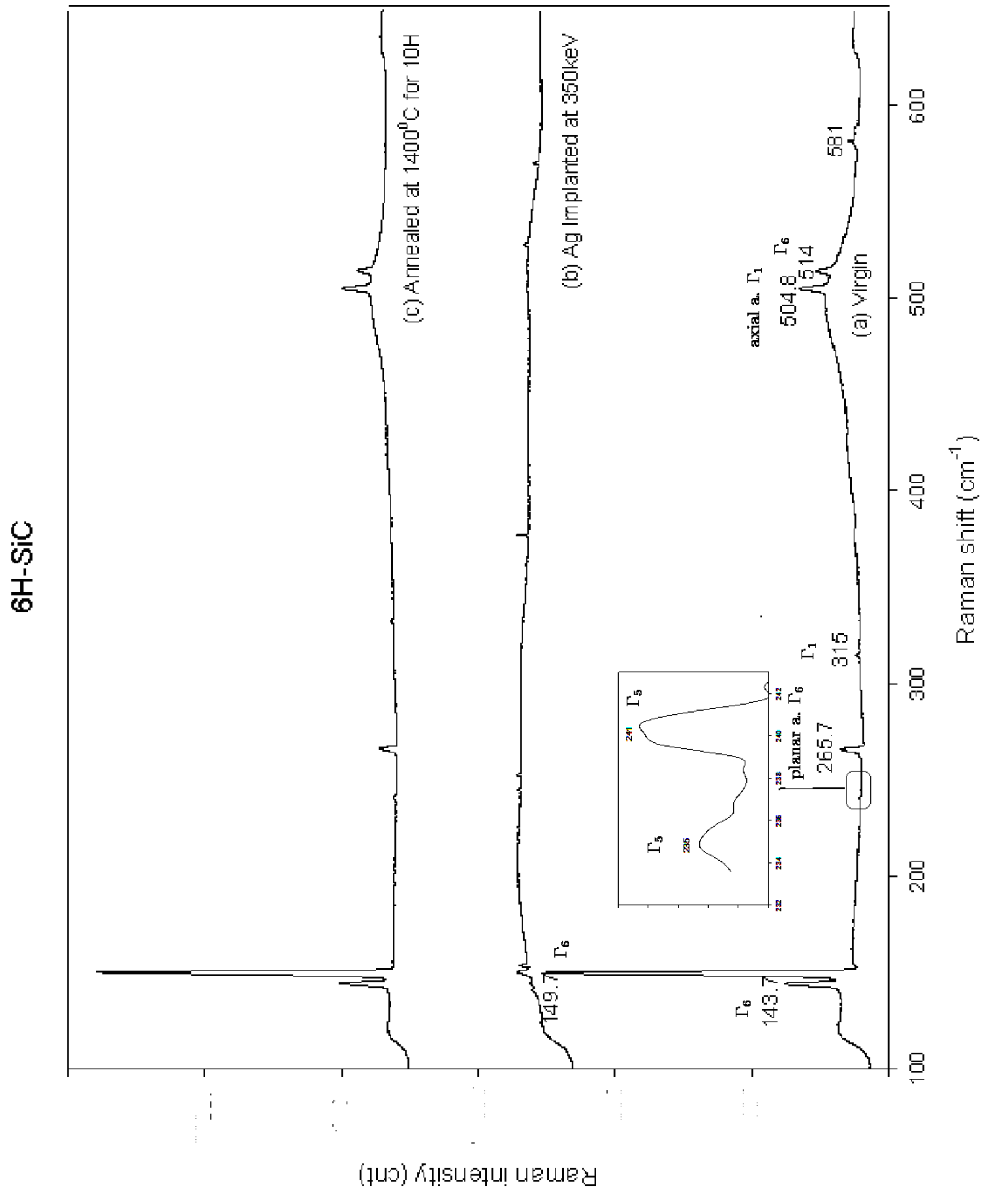

Figure 14: Raman measurements of 6H SiC, region 1

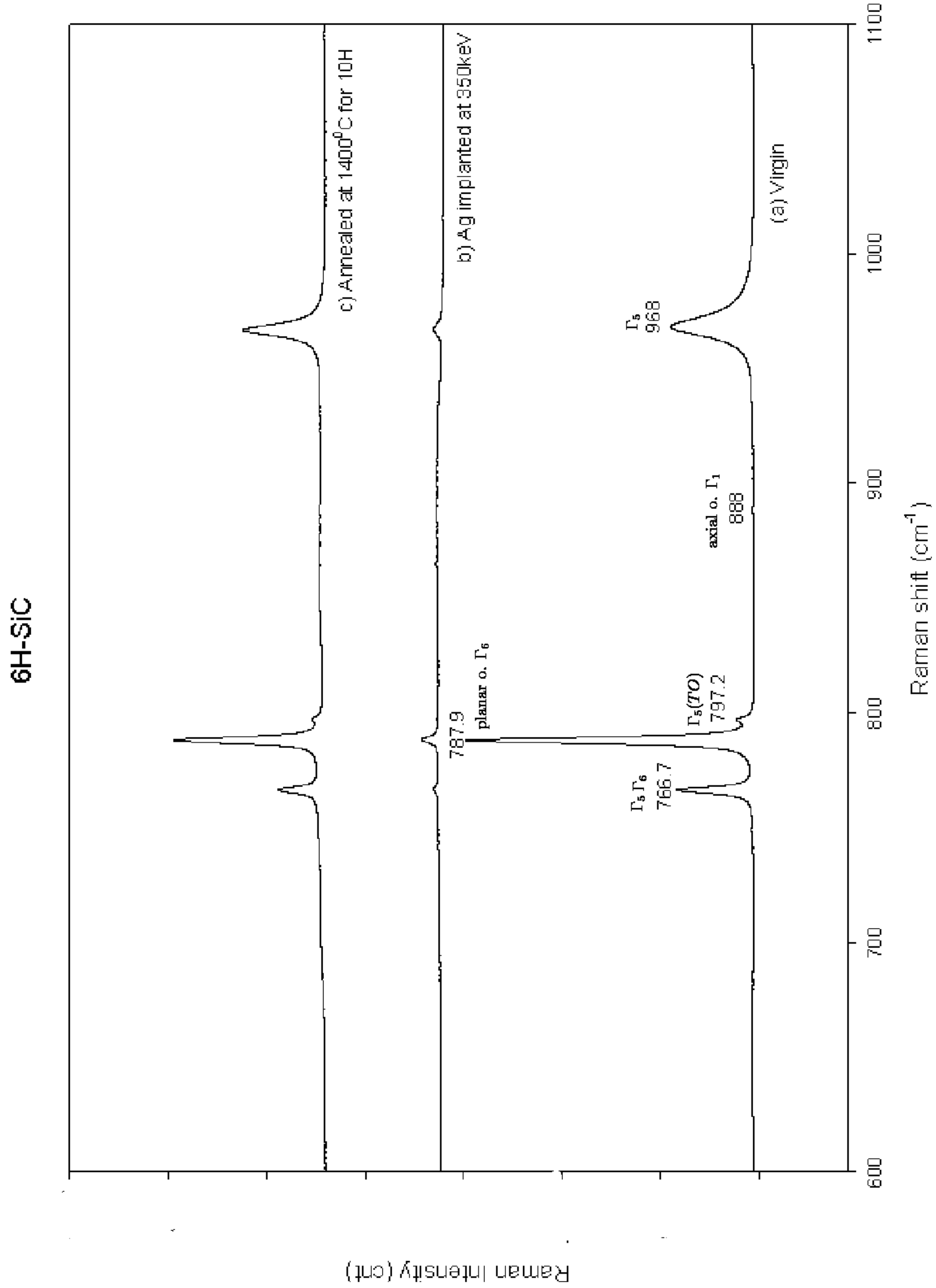

Figure 15: Raman measurements of 6H SiC, region 2

Now we consider the second order Raman effect which is a scattering process where two phonons participate. These two phonons yields: Stokes component if both phonons are created, stokes or anti-stokes if one phonon is created and the other is destroyed and if both are destroyed, we end up having anti - stokes component only [24]. The second-order Raman active modes are the overtones and combinations of the first order Raman active modes obtained in Table 11. For them to be overtones, they have to satisfy group theoretical selection rules[28]. Overtones are determined by irrps of modes contained in the Symmetrized square of the first order Raman active modes. If one of the four first Raman modes or one of the twelve folded mode is contained in Symmetrized square, then the overtone will be allowed if not, then the overtone is not allowed.

Consider a two phonon process in GaN tabulated by Kunert [29] which shows all possible overtones and combinations.

Table 12: Two phonons process in Wurtzite C_{6v}^4

Species	Activity	Overtones
$[\Gamma_1]_{(2)}$	D, R	$2\Gamma_1$(LO) or $2\Gamma_1$(TO)
$[\Gamma_5]_{(2)}$	D, R	$2\Gamma_5$(LO) or $2\Gamma_5$(TO)
$[\Gamma_6]_{(2)}$	D, R	$2\Gamma_6$(LO) or $2\Gamma_6$(TO)
Combinations		
$\Gamma_1 \otimes \Gamma_5$	D, R	Γ_1(LO) + Γ_5(LO) or Γ_1(LO) + Γ_5(TO) or Γ_1(TO) + Γ_5(LO) or Γ_1(TO) + Γ_5(TO)
$\Gamma_1 \otimes \Gamma_6$	D, R	Γ_1(LO) + Γ_6(low) or Γ_1(LO) + Γ_6(high) or Γ_1(TO) + Γ_6(low) or Γ_1(TO) + Γ_6(high)
$\Gamma_1 \otimes \Gamma_6$	D, R	Γ_5(LO) + Γ_6(low) or Γ_5(LO) + Γ_6(high) or Γ_5(TO) + Γ_6(low) or Γ_5(TO) + Γ_6(high)

There are also three phonons modes where the overtones and combinations of GaN tabulated with their frequencies in table 2 by Kunert [29] .
From the Kunert [29], we can have the following overtones and combinations:

(i) Three phonon overtones are $3\Gamma_1(TO)$, $3\Gamma_1(LO)$, $3\Gamma_5(TO)$, $3\Gamma_5(TO)$, $3\Gamma_6(low)$ and $3\Gamma_6(high)$.

(ii) Simple combinations are $\Gamma_1 \otimes \Gamma_5 \otimes \Gamma_6$ which resulting phonon energy such as: $\Gamma_1(TO) \otimes \Gamma_5(TO) \otimes \Gamma_6(low)$, $\Gamma_1(TO) \otimes \Gamma_5(TO) \otimes \Gamma_6(high)$, $\Gamma_1(TO) \otimes \Gamma_5(LO) \otimes \Gamma_6(low)$, $\Gamma_1(TO) \otimes \Gamma_5(LO) \otimes \Gamma_6(high)$, $\Gamma_1(LO) \otimes \Gamma_5(TO) \otimes \Gamma_6(low)$, $\Gamma_1(LO) \otimes \Gamma_5(TO) \otimes \Gamma_6(high)$, and so on.
(iii) General combinations such as: $[\Gamma_1]_{(2)} \otimes \Gamma_5$, $[\Gamma_1]_{(2)} \otimes \Gamma_6$, $[\Gamma_5]_{(2)} \otimes \Gamma_1$, $[\Gamma_5]_{(2)} \otimes \Gamma_6$, $[\Gamma_6]_{(2)} \otimes \Gamma_1$, and so on.

For 6H SiC, the overtones and combinations are similar to the one of GaN as both material follows the same selection rules for C_{6v}^4 space group.

Figure 16 exhibits the second and third order Raman active modes which are overtones or combinations of the first order and folded Raman active modes as stated above. We are going to use the table of phonon frequencies by Kunert et.al [27] as the reference.
As to check the surface and structure of the material, the same 6H-SiC were treated with ion implantation. Ion implantation results in damaging the lattice and form some defects. To repair the damage, the material should be annealed at different temperature.

The Raman spectra of Ag implanted at 350keV and annealed 6H-SiC are presented in figure 14, 15 and 16 . The energy and the fluence of the implanted ions and thermal history of the sample determines the measured spectra.
In figure 14, the folded modes which are having a sharp peak at that region for an untreated material have disappear due to ion implantation and were also recovered by the process of annealing at 1400 ^oC for 10H. Similarly for region 3, the combinations and overtones modes peaks appearing on untreated modes disappeared due to ion implantation and also recovered by annealing process.

In figure 15, the first Raman modes didn't disappear completely as there are the strong peak but the intensity was reduced. After annealing process, the Intensity turn to increases which really shows the recovery of crystallinity.

Raman scattering which is the inelastic scattering of monochromatic light by vibrational modes of the sample has proven to give additional insight into the recrystallization behavior of ion damaged materials.

Table 13: Phonons frequencies of 6H - SiC $(in \pm 5\, cm^{-1})$ zone center modes from Raman measurements by Kunert et. al[27]

Second - order modes [29]	Possible assignments	Experimental measured energy (cm^{-1})
1470		1479
1516 ⇒	$3\Gamma_1$ (504)	1515.5
1532		1532
1542 ⇒	$3\Gamma_1$ (514)	1544
1614		1616
1626 ⇒	$889 + 504 + 236$ combinations	1626
1651 ⇒	$889 + 515 + 241$ combinations	1650
1686		1685
1714		1713.5
1925 ⇒	$2\Gamma_1$(LO)	?

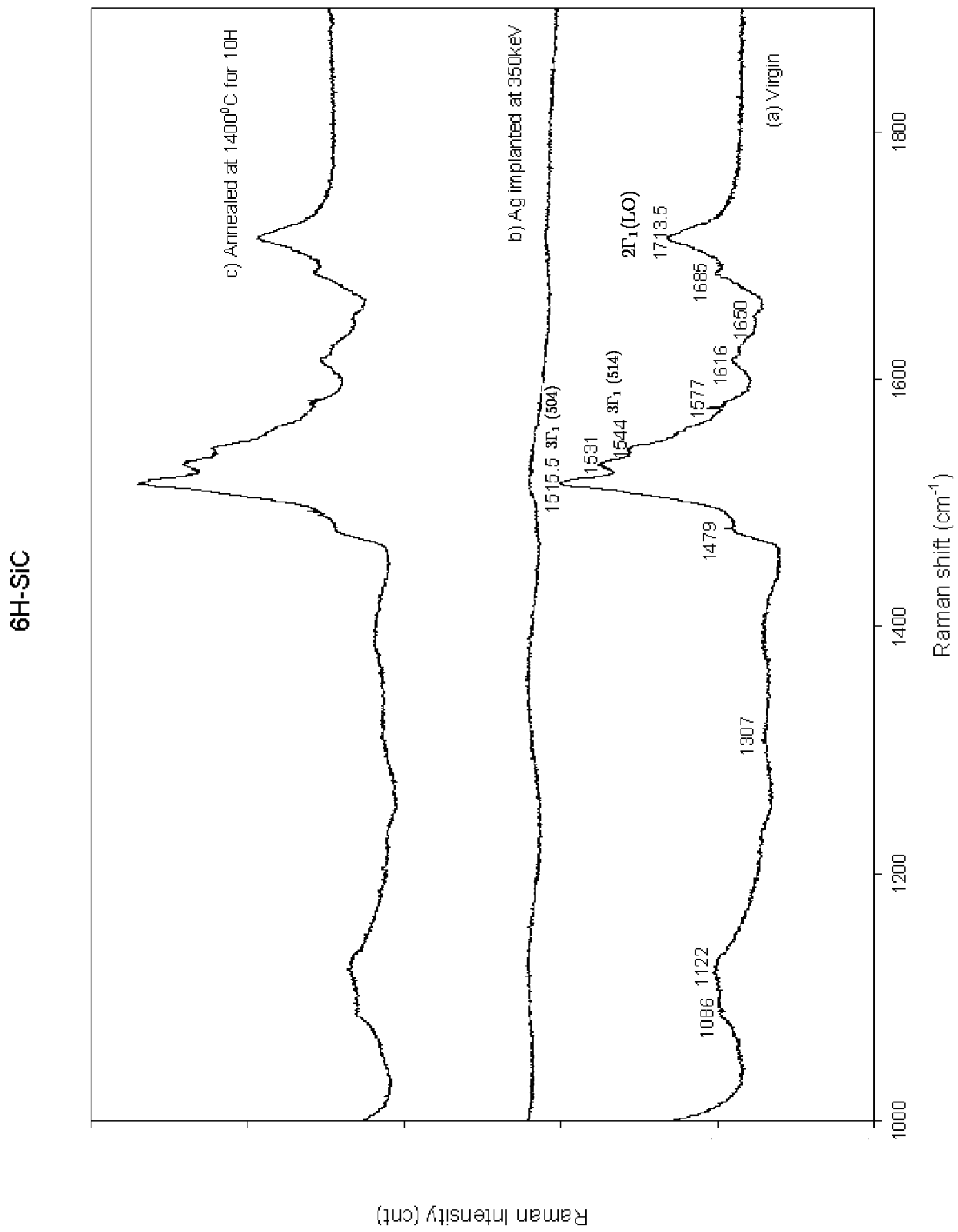

Figure 16: Raman measurements of 6H SiC, region 3

4.2 Infrared spectroscopy

The structure or surface of untreated and treated 6H - SiC were investigated using Fourier Transform Infrared Reflectance(FTIR). Figure 17 exhibits the measurement done by FTIR technique on different surface of the material. The IR active modes of 6H - SiC are presented by Patrick [30] as Γ_1 at $x = 0.67$ and Γ_5 at $x = 0$.
The reststrahl band appearing between $700\,cm^{-1}$ and $1000\,cm^{-1}$ is associated with the transverse optical (TO) phonon frequency. The falling edge beyond the high frequency is associated with the longitudinal optical (LO) phonon frequency. [31],[32]
The height and the shape of reststrauhlung band are affected by implantation damage and are also often used to monitor the recovery of radiation damaged material during thermal annealing.

The spectra of implanted sample shows an asymmetric depletion of the reststrahl band. The spectra of the annealed sample shows the recovery of the crystallinity as the reststrahl band regain its height and shape.

Figure 17 exhibits also can prove the damaged done by ion implantation and a recovery of the structural from the annealing process as it had been presented in Raman Spectra.

Infrared spectroscopy is also another technique which can be used to check the structural changes of the untreated and treated materials.

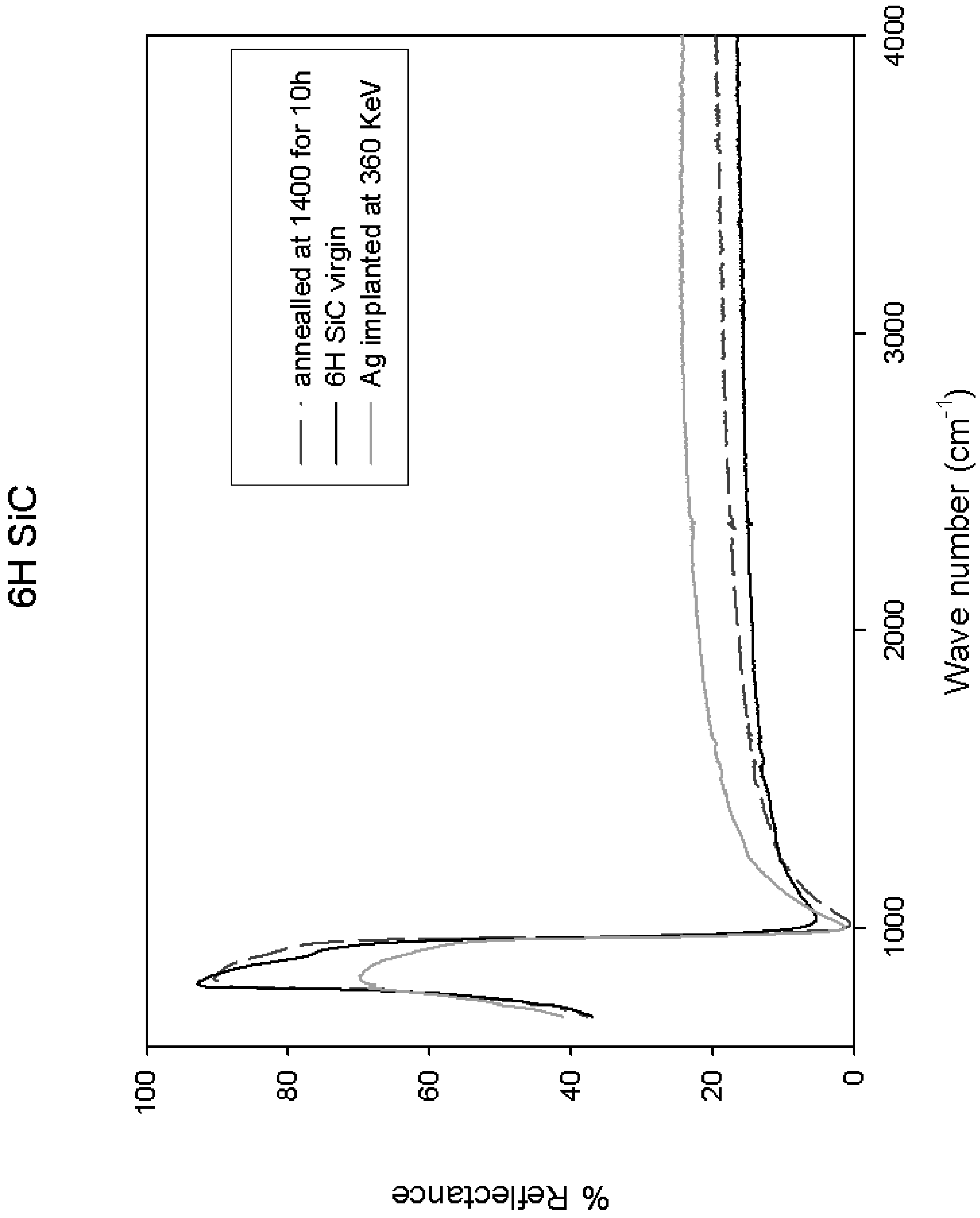

Figure 17: Infrared spectroscopy measurements of 6H SiC

4.3 Photoluminescence

The same crystals of 6H - SiC were investigate by low temperature PL using 514nm Ar laser as excitation source. Using this technique we managed to monitored the structural changes of a different samples which are untreated material , Ag implanted and annealed at 1400 ^{o}C.

Figures 18 exhibits the PL spectra of the high energy. The sharp peaks are observed for the untreated and annealed material at photon energy between 2.96 eV and 3.0 eV without phonon replica. The spectra shows prominent peaks which are phonons replica at photon energies between 2.88 eV and 2.96 eV.

Ion implantation changes crystal quality of the sample at a different dose [33]. A dose of $2 \times 10^{16}\, cm^{-2}$, was used to irradiate the samples and shows the damage and changing of the crystallinity of the sample to an amorphous state having evidently proved with the PL spectra of Ag implanted since most of the peaks disappeared.

By annealing the sample as already stated earlier, the sample recover its crystallinity as the annealing temperature increases. The PL spectra of annealed sample is also presented in the same figure which shows the recovering of the sharp peaks and phonons replica which was found on the virgin sample. Figure 18 also shows the defects of Ag implantation at photon energy of 2.95 eV.

The annealing of the sample from room temperature to high temperature shows the different PL spectra which indicate the involvement of impurities in many of the luminescence centers [34]. Peaks which appears between 2.7 eV and 2.84 eV are related to radiation defects or Ag implantation. Similar case was presented by Peppermuller et al. [35] with 6H-SiC samples after implantation of either boron or hydrogen.

Figure 19 exhibits the low energy PL spectra, where the different materials shows their properties. The spectra of annealed shows the Yellow Light band centering at about 2.3 eV and some distortion band. At low implantation dose and high annealing temperature the Yellow Light band is created.

The band is associated with deep levels involving boron acceptor and eventually alpha particle at rest. Same results were presented by Kunert et al. [27]. The measurement done by the PL shows the same effects in Ag implantations and annealed at a different temperature sample.

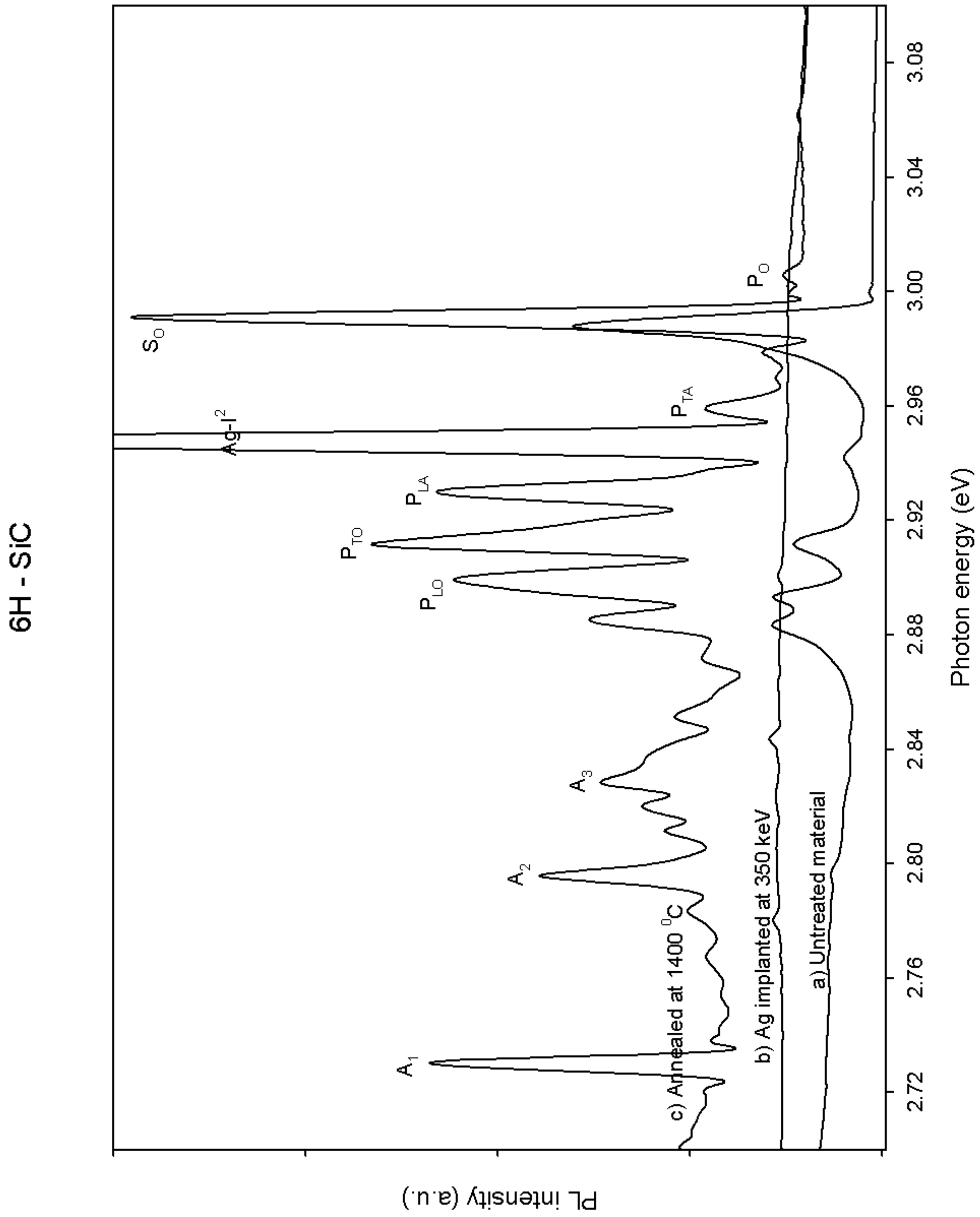

Figure 18: Photoluminescence measurements of 6H SiC, region 1

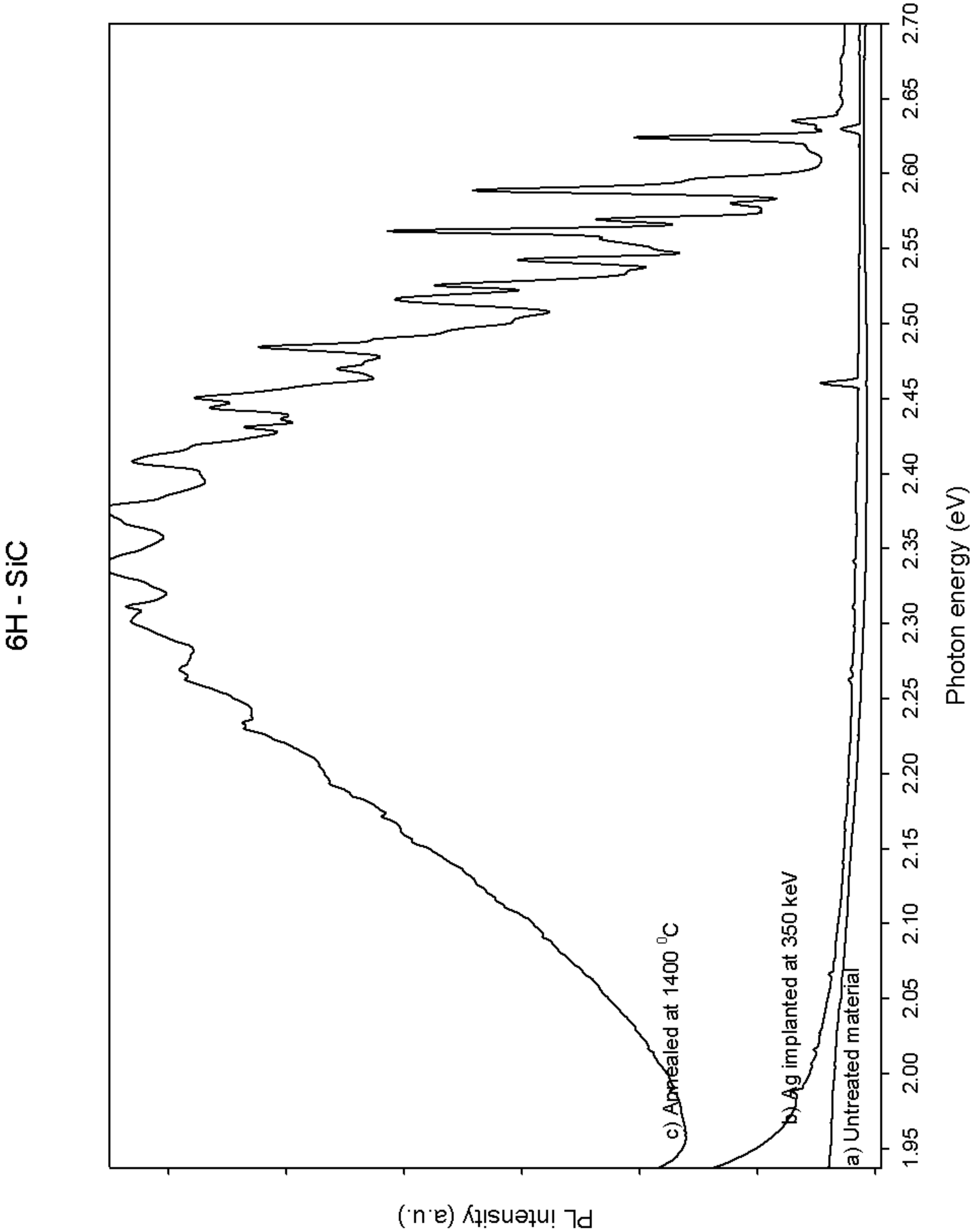

Figure 19: Photoluminescence measurements of 6H SiC, region 2

5 Conclusions

Lattice vibrations of the crystals are characterized by phonons. Lattice vibrations in a crystals having any symmetry can be easily calculated using the Group theory approach. The phonons modes of a semiconductor having the symmetry of C_{6v}^{4} space group were calculated theoretical. The allowed modes of the semiconductor were presented and there was a correlation between the experiments measurements done by different techniques such as: Inelastic X-Ray, time-of-flight neutron scattering done by Nipko, Thoma, Hewat and Ruf. These techniques cannot measure the phonons frequencies at the center of the BZ ($k \cong 0$).

The phonons modes at region $\Gamma \longrightarrow \Delta \longrightarrow A$ were treated under time reversal symmetry (TRS). The experiment measurements done using Inelastic X-Ray, time-of-flight neutron scattering also proves the presence of time reversal symmetry at that region. Two phonons from high symmetry point Γ passing via high symmetry line Δ joins each other at high symmetry point A.
The calculated results also shows that, the two phonons of Δ line are associated with the representation joint $A \oplus A^{*}$.

Raman and Infrared scattering can manage to probe phonons frequency at the center of BZ. To do that, we need to know which modes are Raman and Infrared active. Selection rules for which modes are Raman active it can also be determined using the group theoretical approach. Here we have to determine which representation are contained in the symmetrized KP. The Raman modes were used to characterize the surface of the treated and untreated material (Ag implanted and annealed at $1400\,^{o}C$ for 10H).

The different degrees of damage such as lattice distortion, amorphization and chemical arrangement of a crystal caused by the ion implantation can be detected by Raman, Infrared and photoluminescence spectroscopy. The Raman spectra show the lattice distortion and chemical arrangement. Infrared spectra show the formation of the surface layers and allow the evaluation of the dielectric constants. The annealing process at different temperature could evidently show the recovery of the crystal surface or structure.

References

[1] K. Karch, J.M. Wagner, F. Bechstedt; Phys. Rev. B, **57**,12 (1998)

[2] X.B. Chen, L. Qi,Q Jing, G. Li, W.K Wang, R. P Liu; Sol. Stat. Comm. **45**, 267 - 270 (2007)

[3] K. Karch, F. Bechstedt, Phys. Rev. B **53**, 20 (1996)

[4] S. J. Pearton, Y. D. Park, C.R. Abernathy, M. E Overberg; Thin Soi. Films **447-448**, 493 - 501 (2004)

[5] A Debernardi; Supperlattices Microstruct. **40**, 530 - 532 (2006)

[6] F Tuomisto, D. C. Look, G. C Farlow, Physica. **401 - 402**, 604 - 608 (2007)

[7] H. W. Kunert; Appl. Sur. Sci. **212 - 213** , 890 - 896(2003)

[8] A. P. Cracknell, B. L. Davies, S. C. Miller, W. F. Love; Kronecker products tables(1F1/Plenum, New York, Washington, London, 1979)

[9] M Hamermesh; Group Theory and its Application to Physical Problems, Pergamon Press, New York (1962)

[10] E. I. Rashba; Fiz Tverd. Tela. 1, 407 (1959). English transl: Phys. Solid state **1**, 386 (1959)

[11] P. Lyle, D. R. Hamilton, W. J. Choyke; Phys. Rev. **143**, 526 (1996)

[12] H. W. Kunert; Eur. Phys. J. Appl. Phys. **27**, 251-254 (2004)

[13] A. G. J. Machatine, H. W. Kunert, A. Hoffmann, J. B. Malherbe, J. Barnas, R. Seguin, M. R. Wagner, P. Niyongabo, N Nephale; J. Phys. Conf: Ser. **92**, 012071 (2007)

[14] J.C. Nipko, C. K. Loong, C. M. Balkas, R. F. Davies; Appl. phys. Lett. **73**, 34 (1998)

[15] G.L. Bir, G.E. Pikus; Symmetry and Strain-Induced Effects in Semiconductors, John Wiley and Sons Inc. (1974)

[16] H. W. Kunert, K. Osuch, J. Barnas; Supperlattices Microstruct. **38** , 329 - 335 (2005)

[17] G. Forbenius and I. Schur Berl. Ber. 186 (1906)

[18] A. Hewat; Sol. Stat. Comm. **8**, 187 - 189 (1970)

[19] K. Thoma, B. Dorner, G. Duesig, W. Wegner; Sol. Stat. Comm. **15** , 1111 - 1114 (1974)

[20] T. Ruf, J. Serrano, M. Cardona; Phys. Rev. Lett. **86**, 5 , 906 (2000)

[21] R. Loudon; Royal Society of London, Series A, Mathematical and Physical Science, Vol 275, No 1361, 218 - 232 (1963)

[22] A. W. Joshi; Elements of Group Theory for Physicists, J. Wiley and Sons Inc. (1982)

[23] S. Nakashima, H. Harma; Phys. stat. sol (a) 162, 39 (1997)

[24] R. Loudon, Raman Effect in Crystals, Royal Radar Establishment, Malvern, Worcs

[25] R. Saito, G. Dresselhaus, M. S. Dresselhaus; Physical Properties of Carbon Nanotubes (1998)

[26] M. Hofmann, A. Zywietz, K. Karch, F. Bechstedt; Phys. Rev. B, **18**, 50 (1994)

[27] H. W. Kunert, T. Maurice, J. Barnas, J. Malherbe, D. J. Brink, L. Prinsloo; Vacuum **78**, 503 - 508 (2005)

[28] J. Birman; Phys. Rev. **131**, 1489 (1963)

[29] H. W. Kunert; Supperlattices Microstruct. **36** , 651 - 658 (2004)

[30] L. Patrick; Phys. Rev. **167**, 3, 809 (1968)

[31] Z.C Feng, S.C Lien, J. H Zhao, X W Sun, W Lu; Thin Solid films (2007), doi:10.1016/j.tsf.2007.07.094

[32] H. Houbert, H. Dunken, R. Menzel, T. Bachmann, W. Wesch; Journal of Non - Crystalline Solids **220**, 187-194 (1997)

[33] H.W. Kunert, T. P. Maurice, D.J. Brink, L.C. Prinsloo, J. B Malherbe, J Cammessel, Nucl. Instrum. Methods Phys. Res. B, **181**, 286 - 292 (2001)

[34] L. Patrick, W. J. Choyke, Phys. Rev. B, **5** 8 (1971)

[35] C. Peppermuller, R. Helbig, K. Rottner, A. Schoner; Appl. Phys. Lett. **70**, 8 ,24 (1996)

Appendix

1. Normal modes

The following are the calculation of Normal modes spanned by DR at critical high symmetry points and lines in C_{6v}^{4} wurtzite:

Using the formulated reduction formula:

$$a_{\Gamma_i} = \frac{1}{g}\sum_i \chi^{DR}\left(g/\tau_g\right)\chi^{\Gamma_i}\left(/\tau_g\right) \tag{18}$$

where (g/τ_g) is 1, 2.1, 3, 4.1, 5, 6.1, 19, 20.1, 21, 22.1, 23, and 24.1, and i = 1, . . . , 6 and χ^{DR} is the characters of DR and chi^{Γ_i} is the characters of Γ which are presented in table 1 (section 2.1)

We are only going to use operator 1, 19, 21, 23 as the other ones turns to zero.

$a_{\Gamma_1} = \frac{1}{12}\left[12(1) + 4(1) + 4(1) + 4(1)\right] = 2$

$a_{\Gamma_2} = \frac{1}{12}\left[12(1) + 4(-1) + 4(-1) + 4(-1)\right] = 0$

$a_{\Gamma_3} = \frac{1}{12}\left[12(1) + 4(-1) + 4(-1) + 4(-1)\right] = 0$

$a_{\Gamma_4} = \frac{1}{12}\left[12(1) + 4(1) + 4(1) + 4(1)\right] = 2$

$a_{\Gamma_5} = \frac{1}{12}\left[12(2) + 4(0) + 4(0) + 4(0)\right] = 2$

$a_{\Gamma_6} = \frac{1}{12}\left[12(1) + 4(0) + 4(0) + 4(0)\right] = 2$

Therefore $\Gamma : 2\Gamma_1 \oplus 2\Gamma_4 \oplus 2\Gamma_5 \ \oplus 2\Gamma_6$

Using table 2 (for χ^{K}) from section 2.1 for character of high symmetry point K and formulated reduction formula 19

$$a_{\Gamma_i} = \frac{1}{g} \sum_{i} \chi^{DR} \left(g/\tau_g\right) \chi^{\Gamma_i} \left(g/\tau_g\right) \tag{19}$$

where (g/τ_g) is 1, 3, 5, 20.1, 22.1, and 24.1, and i = 1, . . . , 3

$a_{K_1} = \frac{1}{6}\left[12(1) + 0(1) + 0(1) + 0(1) + 0(1) + 0(1)\right] = 2$

$a_{K_2} = \frac{1}{6}\left[12(1) + 0(1) + 0(1) + 0(1) + 0(1) + 0(1)\right] = 2$

$a_{K_3} = \frac{1}{6}\left[12(2) + 0(1) + 0(1) + 0(1) + 0(1) + 0(1)\right] = 4$

Therefore $K : 2K_1 \oplus 2K_2 \oplus 4K_3$

Using table 3 ($\chi^{\sum}$) from section 2.1 for high symmetry line $\sum$ and formulated reduction formula 20

$$a_{\sum_i} = \frac{1}{g} \sum_{i} \chi^{DR} \left(g/\tau_g\right) \chi^{\sum_i} \left(g/\tau_g\right) \tag{20}$$

where (g/τ_g) is 1 and 24.1, and i = 1,2

$a_{\sum_1} = \frac{1}{2}\left[12(1) + 4(1)\right] = 8$

$a_{\sum_1} = \frac{1}{2}\left[12(1) + 4(-1)\right] = 4$

Therefore $\sum : 8\sum_1 \oplus 4\sum_2$

By repeating the same calculations for all other points, we can manage to complete the table 4 shown in section 2.1.

2. **Vector representations(VR)**

Using the table 10, chapter 2, section 2.4 (third row) for χ^{VR}, table 1 section 2.1 for χ^{Γ} and formulated reduction formula 21, we can decompose irrps that are contained in VR.

$$a_{\Gamma_i} = \frac{1}{g}\sum_{i} \chi^{VR}\left(g/\tau_g\right)\chi^{\Gamma_i}\left(g/\tau_g\right) \tag{21}$$

where (g/τ_g) is 1, 2.1, 3, 4.1, 5, 6.1, 19, 20.1, 21, 22.1, 23, and 24.1, and i = 1, . . . , 6

$a_{\Gamma_1} = \frac{1}{12}[3(1) + 2(1) + 0(1) + (-1)(1) + 0(1) + 2(1) + 1(1)+$

$1(1) + 1(1) + 1(1) + 1(1) + 1(1) = 1$

$a_{\Gamma_2} = \frac{1}{12}[3(1) + 2(1) + 0(1) + -1(1) + 0(1) + 2(1) + 1(-1)+$

$1(-1) + 1(-1) + 1(-1) + 1(-1) + 1(-1) = 0$

$a_{\Gamma_3} = \frac{1}{12}[3(1) + 2(-1) + 0(1) + -1(-1) + 0(1) + 2(-1) + 1(-1)+$

$1(1) + 1(-1) + 1(1) + 1(-1) + 1(1) = 0$

$a_{\Gamma_4} = \frac{1}{12}[3(1) + 2(1) + 0(1) + -1(1) + 0(1) + 2(1) + 1(1)+$

$1(1) + 1(1) + 1(1) + 1(1) + 1(1) = 0$

$a_{\Gamma_5} = \frac{1}{12}[3(2) + 2(-1) + 0(-1) + -1(2) + 0(-1) + 2(-1) + 1(0)+$

$1(0) + 1(0) + 1(0) + 1(0) + 1(0) = 0$

$a_{\Gamma_6} = \frac{1}{12}[3(2) + 2(1) + 0(-1) + -1(-2) + 0(-1) + 2(1) + 1(0) +$

$1(0) + 1(0) + 1(0) + 1(0) + 1(0) = 1$

therefore, we can write:

$\text{VR} = \Gamma_1 \oplus \Gamma_6$

3. Symmetry vector representations

Characters $\chi(g)$ of Twelve Symmetry Operators

$$1 \qquad E \qquad \begin{pmatrix} 1 & 0 & 0 \\ 0 & 1 & 0 \\ 0 & 0 & 1 \end{pmatrix} \qquad Tr(E) = 3$$

$$2 \qquad C_6^+ \qquad \begin{pmatrix} 1 & -1 & 0 \\ 1 & 0 & 0 \\ 0 & 0 & 1 \end{pmatrix} \qquad Tr(C_6^+) = 2$$

$$3 \qquad C_3^+ \qquad \begin{pmatrix} 0 & -1 & 0 \\ 1 & -1 & 0 \\ 0 & 0 & 1 \end{pmatrix} \qquad Tr(C_3^+) = 0$$

$$4 \qquad C_2+ \qquad \begin{pmatrix} -1 & 0 & 0 \\ 0 & -1 & 0 \\ 0 & 0 & 1 \end{pmatrix} \qquad Tr(C_2) = -1$$

$$5 \qquad C_3^- \qquad \begin{pmatrix} -1 & 1 & 0 \\ -1 & 0 & 0 \\ 0 & 0 & 1 \end{pmatrix} \qquad Tr(C_3^-) = 0$$

$$6 \qquad C_6^- \qquad \begin{pmatrix} 0 & 1 & 0 \\ -1 & 1 & 0 \\ 0 & 0 & 1 \end{pmatrix} \qquad Tr(C_6^-) = 2$$

$$19 \qquad \delta_{v1} \qquad \begin{pmatrix} -1 & 1 & 0 \\ 0 & 1 & 0 \\ 0 & 0 & 1 \end{pmatrix} \qquad Tr(\delta_{v1}) = 1$$

$$20 \quad \delta_{d2} \quad \begin{pmatrix} -1 & 0 & 0 \\ -1 & 1 & 0 \\ 0 & 0 & 1 \end{pmatrix} \quad Tr(\delta_{d2}) = 1$$

$$21 \quad \delta_{v3} \quad \begin{pmatrix} 0 & -1 & 0 \\ -1 & 0 & 0 \\ 0 & 0 & 1 \end{pmatrix} \quad Tr(\delta_{v3}) = 1$$

$$22 \quad \delta_{d1} \quad \begin{pmatrix} 1 & -1 & 0 \\ 0 & -1 & 0 \\ 0 & 0 & 1 \end{pmatrix} \quad Tr(\delta_{d1}) = 1$$

$$23 \quad \delta_{v2} \quad \begin{pmatrix} 1 & 0 & 0 \\ 1 & -1 & 0 \\ 0 & 0 & 1 \end{pmatrix} \quad Tr(\delta_{v2}) = 1$$

$$24 \quad \delta_{d3} \quad \begin{pmatrix} 0 & 1 & 0 \\ 1 & 0 & 0 \\ 0 & 0 & 1 \end{pmatrix} \quad Tr(\delta_{d3}) = 1$$

Since the character is the trace of the symmetry operator's matrix representation. The following character table is obtained:

g	1	2	3	4	5	6	19	20	21	22	23	24
$\chi(g)$	3	2	0	-1	0	2	1	1	1	1	1	1

Characters of the Kronecker Product $\chi^2(g)$ of the Symmetry Operators

The character $\chi^2(g)$ is the trace of the (9×9)-matrix obtained after taking the Kronecker product of the symmetry operator's (3×3)-matrix representation. This is the same as squaring the character of the symmetry operator, therefore:

$$[\chi(E)]^2 = [Tr(E)]^2 = 3^2 = 9$$

g	1	2	3	4	5	6	19	20	21	22	23	24
$\chi(g)$	3	2	0	-1	0	2	1	1	1	1	1	1
$\chi^2(g)$	9	4	0	1	0	4	1	1	1	1	1	1

Characters of the Symmetric and Anti-symmetric Product Representations

The symmetric and anti-symmetric product representations are given by (note brackets):

$$\begin{aligned}
[D^{\mu} \otimes D^{\mu}(g)]_{kl,ij} &\Rightarrow \text{symmetric product representation with dimension } \tfrac{1}{2}n_{\mu}(n_{\mu}+1) \\
\{D^{\mu} \otimes D^{\mu}(g)\}_{kl,ij} &\Rightarrow \text{anti} - \text{symmetric product representation with dimension } \tfrac{1}{2}n_{\mu}(n_{\mu}-1)
\end{aligned}$$

Their characters are defined as follows:

$$\begin{aligned}
[\chi \otimes \chi(g)]_{(z)} = \tfrac{1}{2}\left[\chi^2(g) + \chi(g^2)\right] &\Rightarrow \text{character of symmetric product representation} \\
\{\chi \otimes \chi(g)\}_{(z)} = \tfrac{1}{2}\left[\chi^2(g) - \chi(g^2)\right] &\Rightarrow \text{character of anti} - \text{symmetric product representation}
\end{aligned}$$

Using the multiplication table of a space groups, we can determine the squares of the irrps:

g	1	2	3	4	5	6	19	20	21	22	23	24
g^2	1	3	5	1	3	5	1	1	1	1	1	1

Therefore we obtain the following characters table of symmetrized product representations :

g	1	2	3	4	5	6	19	20	21	22	23	24
g^2	1	3	5	1	3	5	1	1	1	1	1	1
$\chi(g)$	3	2	0	-1	0	2	1	1	1	1	1	1
$(\chi(g))^2$	9	4	0	1	0	4	1	1	1	1	1	1
$\chi(g^2)$	3	0	0	3	0	0	3	3	3	3	3	3
$\left[(\chi(g))^2 + \chi(g^2)\right]$	12	4	0	4	0	4	4	4	4	4	4	4
$\frac{1}{2}\left[(\chi(g))^2 + \chi(g^2)\right]$	6	2	0	2	0	2	2	2	2	2	2	2

Determining Symmetries of the Raman-Active Modes

Using formulated reduction formula and the last row on above table, we can manage to find which irreducible representation are symmetrized.

The reduction formula is of the form:

$$a_\mu = \frac{1}{g}\sum_i \left[\chi\left(g/\tau_g\right) \times \chi\left(g/\tau_g\right)\right]_{sym} \chi^{\Gamma_i}\left(g/\tau_g\right) \tag{22}$$

where $\left[\chi\left(g/\tau_g\right) \times \chi\left(g/\tau_g\right)\right]_{sym}$ is the character of the symmetrized VR, χ^{Γ_i} $(i = 1,\ldots,6)$ is the character of the high symmetry point Γ and (g/τ_g) is 1, 2.1, 3, 4.1, 5, 6.1, 19, 20.1, 21, 22.1, 23, and 24.1, and i = 1, . . . , 6

$a_{\Gamma_1} = \frac{1}{12}[6(1) + 2(1) + 0(1) + 2(1) + 0(1) + 2(1) + 2(1) + 2(1) +$

$2(1) + 2(1) + 2(1) + 2(1)] = 2$

$a_{\Gamma_2} = \frac{1}{12}[6(1) + 2(1) + 0(1) + 2(1) + 0(1) + 2(1) + 2(-1) +$

$2(-1) + 2(-1) + 2(-1) + 2(-1) + 2(-1)] = 0$

$a_{\Gamma_3} = \frac{1}{12}[6(1) + 2(-1) + 0(1) + 2(-1) + 0(1) + 2(-1) + 2(-1) +$

$2(1) + 2(-1) + 2(1) + 2(-1) + 2(1)] = 0$

$a_{\Gamma_4} = \frac{1}{12}[6(1) + 2(-1) + 0(1) + 2(-1) + 0(1) + 2(-1) + 2(1) +$

$2(-1) + 2(1) + 2(-1) + 2(1) + 2(-1)] = 0$

$a_{\Gamma_5} = \frac{1}{12}[6(2) + 2(-1) + 0(-1) + 2(2) + 0(-1) + 2(-1) + 2(0) +$

$2(0) + 2(0) + 2(0) + 2(0) + 2(0)] = 1$

$a_{\Gamma_6} = \frac{1}{12}[6(2) + 2(1) + 0(-1) + 2(-2) + 0(-1) + 2(1) + 2(0) +$

$2(0) + 2(0) + 2(0) + 2(0) + 2(0)] = 1$

Finally we can write:

$[V \oplus V]_{(2)} = 2\Gamma_1 \oplus \Gamma_5 \oplus \Gamma_6$